

Theory and modeling of nonperturbative effects in thermoviscous acoustofluidics

Jonas Helboe Joergensen^{*} and Henrik Bruus[†]

Department of Physics, Technical University of Denmark, DTU Physics Building 309, DK-2800 Kongens Lyngby, Denmark

 (Received 22 December 2021; revised 30 October 2022; accepted 2 December 2022; published 24 January 2023)

A theoretical model of thermal boundary layers and acoustic heating in microscale acoustofluidic devices is presented. Based on it, an iterative numerical model is developed that enables numerical simulation of nonlinear thermoviscous effects due to acoustic heating and thermal advection. Effective boundary conditions are derived and used to enable simulations in three dimensions. The theory shows how friction in the viscous boundary layers causes local heating of the acoustofluidic device. The resulting temperature field spawns thermoacoustic bulk streaming that dominates the traditional boundary-driven Rayleigh streaming at relatively high acoustic energy densities. The model enables simulations of microscale acoustofluidics with high acoustic energy densities and streaming velocities in a range beyond the reach of perturbation theory, and is relevant for design and fabrication of high-throughput acoustofluidic devices.

DOI: [10.1103/PhysRevE.107.015106](https://doi.org/10.1103/PhysRevE.107.015106)

I. INTRODUCTION

Modeling and simulations of acoustofluidic devices are used to optimize and develop designs of microscale acoustofluidic devices. Traditionally, acoustofluidic models have been based on perturbation theory [1–8], but in the Letter [9] containing theory and experimental validation and which is jointly submitted with this paper containing the detailed theoretical derivations, we present an iterative numerical model that enables simulations of nonlinear acoustofluidics beyond the amplitude limitations set by perturbation theory. The motivation for this theoretical development is the observation in our previous theoretical and experimental work on thermoacoustic streaming [7,8] that the perturbative treatment is pushed to its limit and beyond when moderate thermal gradients are applied to a standard acoustofluidic device driven in the MHz regime. In such thermoacoustofluidic devices, the perturbation model can easily be challenged by the fast thermoacoustic streaming, which creates a significant convection, and by heating from friction in the viscous boundary layers. None of these effects can be captured by standard perturbation theory.

As we pointed out in Ref. [9], the validity of perturbation theory is mainly challenged in systems with a moderately high acoustic energy density $E_{ac} \gtrsim 400 \text{ J/m}^3$, a desirable regime to work in with applications aspects in mind, as it allows for faster acoustofluidic handling of suspended particles [10] and molecular suspensions [11]. In particular, the volumetric throughput is often a limiting factor for clinical use of acoustofluidic devices [12–15], so it is of general interest to develop a model that allows for simulation of such devices with a high E_{ac} . Notably, $E_{ac} \gtrsim 400 \text{ J/m}^3$ can easily be obtained in standard acoustofluidic devices, for which $E_{ac} \approx$

$10\text{--}50 \text{ J/m}^3 \times [U_{pp}/(1 \text{ V})]^2$ has been reported, U_{pp} being the voltage applied to the transducer [16–19], and higher E_{ac} can be obtained by optimized actuation schemes [20–22], such as $E_{ac} = 1700 \text{ J/m}^3$ reported in Ref. [23].

Nonlinear effects due to fast acoustic streaming have previously been studied numerically in gases with a model using an ideal analytical pressure field [24]. Those models include the nonlinear effects of changing the temperature field by streaming-induced convection, but the nonlinear effect of acoustic heating and nonlinearities in the acoustic fields themselves are not included. We note that the above-mentioned MHz thermoacoustic streaming [7,8] is another example of the growing number of fast (above 1 mm/s) acoustic-streaming phenomena, others being absorption of GHz ultrasound [25] and kHz vibrations of gas bubbles [26] or sharp edges [27].

Numerical models in acoustofluidics can be categorized as inviscid models [3], viscous models [1,5] and thermoviscous models [2,7], as well as full models [1,2] and effective models [5,7]. The viscous models include the full viscous fluid description but assume an adiabatic temperature field governed by the pressure field and typically assume temperature-independent material parameters. The thermoviscous models further include thermal boundary layers, temperature-dependent material parameters, and heating created in the viscous boundary layers. *Full models* require numerical resolution of the thin boundary layers, and they are therefore computationally expensive. In contrast, *effective models* include analytical expressions for the boundary layers, so a fine boundary-layer mesh is avoided, and they therefore enable three-dimensional (3D) simulations.

In this work and Ref. [9], we build on and expand our previous perturbative thermoviscous effective model [7] by including heating due to the acoustic field, and by going beyond perturbation theory with the introduction of an iterative scheme including quasisteady and acoustic fields to allow

*jonashj@fysik.dtu.dk

†bruus@fysik.dtu.dk

for higher acoustic energy densities. Two iterative thermoviscous models are developed and constitute the main result of this work: a nonlinear *full* model and a nonlinear *effective-boundary-layer* model. We have presented the main concepts and the experimental validation of the *full* model in Ref. [9], but here we provide a detailed derivation of it. The two models are only valid when the higher order harmonics are negligible, and the effective boundary conditions are valid only in the limit where the thermal and viscous boundary layers are thin compared to the characteristic length scales of the geometry. The nonperturbative effects are important when either the acoustic energy density E_{ac} is high enough for the frictional heating to create thermoacoustic streaming, as reported in Ref. [9] with $E_{ac} \sim 400 \text{ J/m}^3$, or the streaming velocity is high enough for the convective heat transport to be important as observed in Ref. [8].

The outline of the paper is as follows. In Sec. II the basic assumptions and governing equations are presented. In Sec. III we summarize our recent basic theory of the thermoviscous acoustic fields [7]. In Sec. IV the known theory for the steady mechanical fields [7] is presented, and we develop the theory for the steady temperature fields needed for the present nonperturbative approach and supplement it with the *effective-boundary-layer* model. In Sec. V we develop an iterative procedure for computing nonlinear thermoacoustic effects in a nonperturbative approach, and we briefly explain how to implement it in the software COMSOL Multiphysics [28]. In Sec. VI we validate the *effective-boundary-layer* model, and present three model examples of nonperturbative acoustofluidics in two dimensions, involving respectively internal acoustic heating (Sec. VIA) and thermal properties of the surrounding solids (Sec. VIB) and the fluid (Sec. VIC), as well as one example in three dimensions, involving thermoacoustic streaming driven by absorption of light (Sec. VID). Finally, we conclude in Sec. VII.

II. THEORY AND MODEL ASSUMPTIONS

Based on our previous approach [7], we consider an acoustofluidic device consisting of an elastic solid containing a microchannel filled with a thermoviscous Newtonian fluid and actuated by a piezoelectric transducer at a single frequency in the MHz range. This time-harmonic actuation establishes an acoustic field in the system, which in the fluid, by the internal dissipation and hydrodynamic nonlinearities, results in a time-averaged response that leads to acoustic streaming. For simplicity, the piezoelectric transducer is left out of the analysis and is represented only by an oscillating displacement condition on part of the surface of the elastic solid. The transducer could be taken into account in the numerical model, by extending our previous transducer models [6,22,29] to include temperature and thermal properties.

A. Governing equations

The response of the fluid embedded in the elastic solid to the oscillating-displacement boundary condition is controlled by the hydro-, elasto-, and thermodynamic governing equations of the coupled thermoviscous fluid and elastic solid. The linear elastic solid is described in the Lagrangian picture by

the fields of the density ρ , the displacement \mathbf{u} , the temperature T , and the following material parameters: the longitudinal and transverse sound speeds c_{lo} and c_{tr} , the thermal conductivity k^{th} , the specific heat capacity c_p , the ratio of specific heat capacities $\gamma = c_p/c_v$, the thermal expansion coefficient α_p , and the isentropic and isothermal compressibilities κ_s and κ_T . The velocity field is the time derivative of the displacement field, $\mathbf{v}^{sl} = \partial_t \mathbf{u}$, so no advection occurs, and the governing equations are the transport equations of the momentum density $\rho \partial_t \mathbf{u}$ and temperature T [30,31],

$$\rho \partial_t^2 \mathbf{u} = \nabla \cdot \boldsymbol{\sigma}, \quad (1a)$$

$$\partial_t T + \frac{(\gamma - 1)}{\alpha_p} \partial_t (\nabla \cdot \mathbf{u}) = \frac{\gamma}{\rho c_p} \nabla \cdot (k^{th} \nabla T) + P, \quad (1b)$$

where P is any given external heat power density source, and $\boldsymbol{\sigma}$ is the stress tensor, which for isotropic solids is

$$\boldsymbol{\sigma} = -\frac{\alpha_p}{\kappa_T} (T - T_0) \mathbf{I} + \boldsymbol{\tau}, \quad (2a)$$

$$\boldsymbol{\tau} = \rho c_{tr}^2 [\nabla \mathbf{u} + (\nabla \mathbf{u})^T] + \rho (c_{lo}^2 - 2c_{tr}^2) (\nabla \cdot \mathbf{u}) \mathbf{I}. \quad (2b)$$

The system is excited by a given displacement vector harmonically oscillating with angular frequency ω and amplitude $\mathbf{u}_{exc}(\mathbf{s}_{ext})$ on a part \mathbf{s}_{ext} of the external surface of the solid far from the fluid-solid interface

$$\mathbf{u}(\mathbf{r}, t) = \mathbf{u}_{exc}(\mathbf{s}_{ext}) e^{-i\omega t}, \quad \text{for } \mathbf{r} = \mathbf{s}_{ext}. \quad (3)$$

The fluid is described in the Eulerian picture by the fields of the density ρ , the pressure p , the velocity \mathbf{v} , the temperature T , and the energy per mass unit ϵ , and by the following material parameters: the dynamic and bulk viscosity η and η^b , the thermal conductivity k^{th} , the specific heat c_p , the thermal expansion coefficient α_p , the ratio of specific heats $\gamma = c_p/c_v$, and the isentropic and isothermal compressibilities κ_s and $\kappa_T = \gamma \kappa_s$. The governing equations are the transport equations for the density of mass ρ , momentum $\rho \mathbf{v}$, and internal energy $\rho \epsilon$ [2,31,32],

$$\partial_t \rho = -\nabla \cdot (\rho \mathbf{v}), \quad (4a)$$

$$\partial_t (\rho \mathbf{v}) = \nabla \cdot (\boldsymbol{\sigma} - \rho \mathbf{v} \mathbf{v}), \quad (4b)$$

$$\partial_t \left(\rho \epsilon + \rho \frac{v^2}{2} \right) = \nabla \cdot \left[k^{th} \nabla T + \mathbf{v} \cdot \boldsymbol{\sigma} - \rho \mathbf{v} \left(\epsilon + \frac{v^2}{2} \right) \right] + P, \quad (4c)$$

where P is any given external heat power density source, and $\boldsymbol{\sigma}$ is the stress tensor,

$$\boldsymbol{\sigma} = -p \mathbf{I} + \boldsymbol{\tau}, \quad (5a)$$

$$\boldsymbol{\tau} = \eta [\nabla \mathbf{v} + (\nabla \mathbf{v})^\dagger] + \left(\eta^b - \frac{2}{3} \eta \right) (\nabla \cdot \mathbf{v}) \mathbf{I}. \quad (5b)$$

Pressure p and temperature T are related to the internal energy density ϵ by the first law of thermodynamics, and to the density ρ by the equation of state [2,31,33],

$$\rho d\epsilon = (\rho c_p - \alpha_p p) dT + (\kappa_T p - \alpha_p T) dp, \quad (6a)$$

$$d\rho = -\rho \alpha_p dT + \rho \kappa_T dp. \quad (6b)$$

Like the density, any material parameter q has a tempera-

ture and pressure dependency,

$$\frac{1}{q_0} dq = a_q^T \alpha_p dT + a_q^p \kappa_T dp, \quad (7a)$$

$$a_q^T = \frac{1}{\alpha_p q_0} \left(\frac{\partial q}{\partial T} \right)_p, \quad a_q^p = \frac{1}{\kappa_T q_0} \left(\frac{\partial q}{\partial p} \right)_T, \quad (7b)$$

where q_0 is the unperturbed value of q . Note that here the variables are (T, p) and not (T, ρ) as in Refs. [2,7]. For a pressure change dp accompanied by an adiabatic temperature change $dT = (\gamma - 1) \frac{\kappa_T}{\alpha_p} dp$, the adiabatic pressure dependency of a parameter q is

$$\frac{1}{q_0} dq = a_q^T \alpha_p dT + a_q^p \kappa_T dp = a_q^{p,\text{ad}} \kappa_s p_1, \quad (7c)$$

$$a_q^{p,\text{ad}} = \gamma(\gamma - 1) a_q^T + \gamma a_q^p. \quad (7d)$$

For steady temperature gradients and oscillating thermal boundary layers, a_q^T is relevant, and for bulk adiabatic pressure waves, $a_q^{p,\text{ad}}$ is the relevant quantity. For water at $T = 25^\circ\text{C}$ and using Eqs. (6b) and (7), we compute the dimensionless sensitivities a_q^T , a_q^p , and $a_q^{p,\text{ad}}$ from the T - ρ dependencies of the parameters q listed in Ref. [2]:

$$\begin{aligned} a_\rho^T &= -1, & a_{\kappa_s}^T &= -10, \\ a_\rho^p &= 1, & a_\rho^{p,\text{ad}} &= 1, \\ a_\eta^T &= -88, & a_\eta^{p,\text{ad}} &= -1.3, \\ a_{\eta^b}^T &= -100, & a_{\eta^b}^{p,\text{ad}} &= -1.1, \\ a_{\kappa^{\text{th}}}^T &= 8.4, & a_{\kappa^{\text{th}}}^{p,\text{ad}} &= 2.3. \end{aligned} \quad (8)$$

For η^b , we take only the temperature dependence into account, because we have not found data for the pressure dependence. These temperature dependencies imply that thermal gradients may induce gradients in the listed parameters, including the density and the compressibility. This leads to the appearance of the inhomogeneous acoustic body force \mathbf{f}_{ac} previously studied for both solute- and temperature-induced gradients [7,8,11].

B. Separation of length and time scales

Acoustofluidic devices are typically driven at a frequency f in the range from 1 to 50 MHz. The corresponding fast acoustic time scale t_{ac} is thus

$$t_{\text{ac}} = \frac{1}{\omega} = \frac{1}{2\pi f} = 3\text{--}160 \text{ ns}. \quad (9)$$

The timescale τ associated with the hydrodynamic and thermal flow is slower. Following Ref. [11], we estimate for a typical aqueous suspension in a channel of height $H = 0.5$ mm with kinematic viscosity $\nu = \eta/\rho$, density ρ , and relative density difference $\hat{\rho} = 0.1$ induced by concentration or temperature gradients that the following characteristic timescales are all in the order of 10 ms: thermal relaxation $t_{\text{therm}} = H^2/D^{\text{th}}$, viscous relaxation $t_{\text{visc}} = H^2/\nu_0$, inertial motion $t_{\text{inert}} \approx \sqrt{H/(g\hat{\rho})}$, and steady shear motion $t_{\text{shear}} \approx \nu_0/(H g \hat{\rho})$, and thus τ is

$$\tau \approx t_{\text{therm}} \approx t_{\text{visc}} \approx t_{\text{inert}} \approx t_{\text{shear}} \approx 10 \text{ ms}. \quad (10)$$

The slow thermohydrodynamic and fast acoustic timescales τ and t_{ac} are thus separated by at least four to six orders of

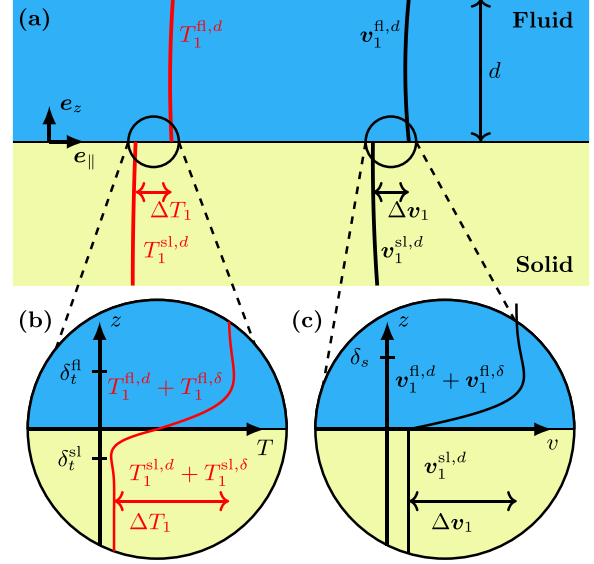


FIG. 1. (a) The temperature $T_1 = T_1^{\text{xl},d} + T_1^{\text{xl},\delta}$ and velocity $\mathbf{v}_1 = \mathbf{v}_1^{\text{xl},d} + \mathbf{v}_1^{\text{xl},\delta}$ across a fluid (xl = fl)–solid (xl = sl) interface with the local normal vector \mathbf{e}_z and the local parallel vector \mathbf{e}_\parallel (either \mathbf{e}_x or \mathbf{e}_y). On the interface, the bulk fields T_1^d and \mathbf{v}_1^d have a discontinuity ΔT_1 and $\Delta \mathbf{v}_1$, respectively, due to the thin thermal ($T_1^{\text{xl},\delta}$) and viscous ($\mathbf{v}_1^{\text{xl},\delta}$) boundary layers. (b) Zoom-in on the thermal boundary layers $T_1^{\text{fl},\delta}$ and $T_1^{\text{sl},\delta}$ with respective thicknesses δ_t^{fl} and δ_t^{sl} . (c) Zoom-in on the viscous boundary layer $\mathbf{v}_1^{\text{fl},\delta}$ in the fluid with thickness δ_s .

magnitude, and we therefore solve the acoustic and steady dynamics separately as in Ref. [11]. In this work we study the steady limit of the slow timescale and describe any given physical field Q_{phys} as a sum of a steady field Q_0 and a time-varying acoustic field $Q_1 e^{-i\omega t}$ with a steady complex-valued amplitude Q_1 ,

$$Q_{\text{phys}}(t) = Q_0 + \text{Re}(Q_1 e^{-i\omega t}). \quad (11)$$

The steady fields set the density and compressibility, which governs the acoustic fields. Conversely, the acoustic fields create an oscillation-time-averaged acoustic body force \mathbf{f}_{ac} and acoustic heating-power density P_{ac} that enter the equations of motion for the steady fields. A time average of a product of two acoustic fields $F_1 e^{-i\omega t}$ and $G_1 e^{-i\omega t}$ is also a steady field, which is given by

$$\langle \text{Re}(F_1 e^{-i\omega t}) \text{Re}(G_1 e^{-i\omega t}) \rangle = \frac{1}{2} \text{Re}(F_1 G_1^*). \quad (12)$$

Here, and in the rest of the work, the asterisk (*) denotes complex conjugation. In contrast to perturbation theory [7], we do not require that Q_1 is much smaller than Q_0 , but we do neglect higher harmonic terms with time dependence $e^{\pm i n \omega t}$, $n = 2, 3, \dots$

Acoustofluidic systems exhibits dynamics on two length scales, one set by the wavelength of the acoustic fields, and one set by the viscous and thermal boundary layers. The boundary conditions on the velocity field, stress, heat flux, and thermal field at the fluid-solid interface result in the appearance of thermal boundary layer of width δ_t in both the fluid and the solid, and in a viscous boundary layer of width δ_s in the fluid; see Fig. 1. These boundary layers are localized near fluid-solid interfaces, and their dynamically defined widths

are small compared to a typical device size or wavelength d [31],

$$\delta_s = \sqrt{\frac{2\nu}{\omega}}, \quad \delta_t = \sqrt{\frac{2D^{\text{th}}}{(1-X)\omega}} \approx \sqrt{\frac{2D^{\text{th}}}{\omega}}, \quad (13)$$

where $D^{\text{th}} = \frac{k^{\text{th}}}{\rho c_p}$ and X is a nondimensional parameter, $X = 0$ for fluids and $X = (\gamma - 1) \frac{4c_p^2}{3c_{10}^2} \lesssim 0.01$ for solids. Typically, $\delta_t \lesssim \delta_s \lesssim 500$ nm, more than two orders of magnitude smaller than $d \sim 100$ μm . We introduce the usual complex wave numbers k_s and k_t associated with the boundary-layer widths δ_s and δ_t , respectively,

$$k_s = \frac{1+i}{\delta_s}, \quad k_t = \frac{1+i}{\delta_t}. \quad (14)$$

In our analysis, the timescale separation (11) of a given field Q into a steady (subscript 0) and an acoustic (subscript 1) field is followed by a length-scale separation into bulk (superscript d) and boundary-layer fields (superscript δ), such that Q is represented by four fields,

$$Q_0 = Q_0^d + Q_0^\delta \quad \text{and} \quad Q_1 = Q_1^d + Q_1^\delta. \quad (15)$$

The bulk and boundary-layer fields are governed by separate governing equations, but they are connected by the boundary conditions at the fluid-solid interface. The boundary fields Q^δ are solved analytically and enter the final model only through effective boundary conditions on the bulk fields Q^d as in [5,7].

In the following, when needed for clarity, we use superscripts “fl” and “sl” to designate properties of the fluids and the solids, respectively. When the context is clear, we often suppress these superscripts to increase the readability of the equations.

C. Boundary conditions

In the usual Lagrangian picture [7], the instantaneous position s at time t of the oscillating fluid-solid interface is given by $s(s_0, t) = s_0 + s_1(s_0)e^{-i\omega t}$, where s_0 is the equilibrium position and s_1 the acoustic displacement around s_0 . The velocity \mathbf{V}^0 of the interface is thus $\mathbf{V}^0(s_0, t) = \partial_t s = \mathbf{V}_1^0 e^{-i\omega t}$ with amplitude $\mathbf{V}_1^0 = -i\omega s_1(s_0)$. The superscript “0” denotes any field defined on the fluid-solid interface. On the solid-fluid interface, the no-slip and continuous stress conditions apply as in Ref. [7], Eqs. (10) and (11). The velocity of the solid wall at a given time and position must equal the Eulerian-picture fluid velocity \mathbf{v}^{fl} ,

$$\mathbf{v}^{\text{fl}}(s_0 + s_1 e^{-i\omega t}, t) = \mathbf{V}_1^0(s_0) e^{-i\omega t} = -i\omega \mathbf{u}_1^0(s_0) e^{-i\omega t}. \quad (16)$$

This boundary condition must be obeyed separately for the steady and acoustic fields (subscript 0 and 1, respectively), so a Taylor expansion yields

$$\mathbf{v}_0(s_0) = -\langle (s_1 \cdot \nabla) \mathbf{v}_1 \rangle|_{s_0}, \quad (17a)$$

$$\mathbf{v}_1(s_0) = \mathbf{V}_1^0(s_0). \quad (17b)$$

Similarly, at a given position on the fluid-solid interface with surface normal \mathbf{n} , the stress $\boldsymbol{\sigma}$ must be continuous,

$$\boldsymbol{\sigma}_0^{\text{sl}}(s_0) \cdot \mathbf{n} = \boldsymbol{\sigma}_0^{\text{fl}}(s_0) \cdot \mathbf{n} + \langle (s_1 \cdot \nabla) \boldsymbol{\sigma}_1^{\text{fl}}(s_0) \cdot \mathbf{n} \rangle|_{s_0}, \quad (18a)$$

$$\boldsymbol{\sigma}_1^{\text{sl}}(s_0) \cdot \mathbf{n} = \boldsymbol{\sigma}_1^{\text{fl}}(s_0) \cdot \mathbf{n}. \quad (18b)$$

Since the viscosity parameters η and η^b depend on the temperature, the explicit expressions of the two stress boundary conditions contain several terms.

Following Ref. [7], two sets of thermal boundary conditions must be imposed. Similar to the velocity, the temperature must be continuous across the solid-fluid interface. This condition must be obeyed separately in the steady and acoustic fields,

$$T_0^{\text{sl}}(s_0) = T_0^{\text{fl}}(s_0) + \langle s_1 \cdot \nabla T_1^{\text{fl}} \rangle|_{s_0}, \quad (19a)$$

$$T_1^{\text{sl}}(s_0) = T_1^{\text{fl}}(s_0). \quad (19b)$$

Similar to the stress, the normal component $-k^{\text{th}} \mathbf{n} \cdot \nabla T$ of the heat flux must be continuous across the interface,

$$-k^{\text{th,sl}} \mathbf{n} \cdot \nabla T^{\text{sl}}(s_0, t) = -k^{\text{th,fl}} \mathbf{n} \cdot \nabla T^{\text{fl}}(s_0 + s_1 e^{-i\omega t}, t). \quad (20)$$

We follow Eq. (7a) and expand $k^{\text{th,sl}} \approx k_0^{\text{th,sl}} + k_1^{\text{th,sl}}$ with $k_1^{\text{th,sl}} = (\partial_T k_0^{\text{th,sl}}) T_1$, but neglect the tiny gradients in \mathbf{n} and s_1 . The boundary conditions of the steady (T_0^{sl}) and acoustic (T_1^{sl}) parts of the heat flux thus become

$$\begin{aligned} & -k_0^{\text{th,sl}} \mathbf{n} \cdot \nabla T_0^{\text{sl}}(s_0) - \langle k_1^{\text{th,sl}} \mathbf{n} \cdot \nabla T_1^{\text{sl}}(s_0) \rangle \\ & = -k_0^{\text{th,fl}} \mathbf{n} \cdot \nabla T_0^{\text{fl}}(s_0) - \langle k_1^{\text{th,fl}} \mathbf{n} \cdot \nabla T_1^{\text{fl}}(s_0) \rangle \\ & \quad - \langle s_1 \cdot \nabla [k_0^{\text{th}} \nabla T_1^{\text{fl}}(s_0)] \cdot \mathbf{n} \rangle, \end{aligned} \quad (21a)$$

$$-k_0^{\text{th,sl}} \mathbf{n} \cdot \nabla T_1^{\text{sl}}(s_0) = -k_0^{\text{th,fl}} \mathbf{n} \cdot \nabla T_1^{\text{fl}}(s_0). \quad (21b)$$

In the following sections, we present and derive the effective boundary conditions for the acoustic and steady fields. In that process a local coordinate system is used at the fluid-solid interface where \mathbf{e}_z is a normal vector of the interface pointing into the fluid, and where \mathbf{e}_x and \mathbf{e}_y are both lying in the interface plane; see Fig. 1.

D. Range of validity of the model

We briefly discuss the range of validity imposed by the main assumptions. First, in this analysis, we study steady and acoustic fields with the actuation frequency ω . So our model is valid only when these fields are much larger than the higher harmonic fields at frequencies $2\omega, 3\omega, \dots$. The amplitudes of the steady \mathbf{v}_0 , the acoustic \mathbf{v}_1 , and the 2ω -harmonic $\mathbf{v}_{2\omega}$ velocities are given in Muller and Bruus [34] as

$$|\mathbf{v}_0| = \frac{Q^2 v_{\text{bc}}^2}{c_s}, \quad |\mathbf{v}_1| = Q v_{\text{bc}}, \quad |\mathbf{v}_{2\omega}| = \frac{Q^3 v_{\text{bc}}^2}{c_s}, \quad (22)$$

where the physical velocity field corresponding to $\mathbf{v}_{2\omega}$ is given as $\mathbf{v}_{2\omega}^{\text{phys}} = \text{Re}[\mathbf{v}_{2\omega} e^{-i2\omega t}]$. Here Q is the quality factor of the resonance peak, given by the full-width-at-half-maximum Γ of the resonance peak as $Q = (2\Gamma)^{-1}$. Our model is valid if $|\mathbf{v}_1|^2 \gg |\mathbf{v}_{2\omega}|^2$, implying an upper bound on the acoustic energy density $E_{\text{ac}} = \frac{1}{4} \rho_0 |\mathbf{v}_1|^2$,

$$E_{\text{ac}} \ll \frac{\rho_0 c_s^2}{4Q^2} \approx 10^3 - 10^5 \text{ J m}^{-3}, \quad (23)$$

where $Q = 100-1000$ is typical for acoustofluidic devices. So in systems with low Q factors the higher order harmonics are important only at very high E_{ac} .

Second, due to low oscillatory advection, we assume $\nabla \cdot (q_0 \mathbf{v}_1) \approx q_0 \nabla \cdot \mathbf{v}_1$, where q_0 is a parameter of the fluid. This requires $|q_0 \nabla \cdot \mathbf{v}_1| \gg |\mathbf{v}_1 \cdot \nabla q_0|$. At room temperature, the validity of our theory is therefore limited by the most temperature-sensitive parameter, the viscosity η_0 ,

$$|\nabla T_0| \ll \left| \frac{\eta_0 k_c}{(\partial_T \eta)_{T_0}} \right| \approx 5000 \frac{\text{K}}{\text{mm}}. \quad (24)$$

In conventional acoustofluidic systems, the temperature gradient is well within this bound, as $|\nabla T_0| \lesssim 50 \text{ K/mm}$.

Third, the effective boundary-layer theory requires the boundary-layer width to be much smaller than both the bulk wavelength, $k_0 \delta \ll 1$, and the radius of curvature R of the fluid-solid interface, $\delta \ll R \simeq d$ (see Sec. II B), which is true for MHz acoustics in water.

III. ACOUSTIC FIELDS

The acoustic part of thermoviscous acoustofluidics is thoroughly studied in Ref. [7] as the first-order fields in the perturbative model. The governing equations of these fields are the same for the perturbative and the iterative model, and therefore the theory from Ref. [7] can be directly applied. This is an effective theory, in which the thermal and viscous boundary layers are given analytically and incorporated in effective boundary conditions on the displacement field $\mathbf{u}_1 = (u_{1,x}, u_{1,y}, u_{1,z})$ and pressure p_1 . The governing equations for the bulk fields and the effective boundary conditions on the solid-fluid boundary are given in Ref. [7], Eqs. (19), (20), (23), (24), and (34), and they are briefly summarized below.

A. Governing equations in the bulk

As shown in Ref. [7], Sec. IV A, the acoustic pressure p_1 in the bulk of the fluid is given by the Helmholtz equation, derived from Eqs. (4) and (5), and the bulk velocity \mathbf{v}_1^d and the adiabatic temperature T_1^d follow from p_1 :

$$\nabla^2 p_1 = -k_c^2 p_1, \quad k_c = \frac{\omega}{c} (1 + i\Gamma_{0c}^{\text{fl}}), \quad (25a)$$

$$\mathbf{v}_1^{d,p} = -i \frac{1 - i\Gamma_{0c}^{\text{fl}}}{\omega \rho_0} \nabla p_1, \quad (25b)$$

$$T_1^d = (\gamma - 1) \frac{\kappa_{s0}}{\alpha_{p0}} p_1. \quad (25c)$$

Further, as shown in Ref. [7] Sec. IV B, the displacement \mathbf{u}_1 in the solid is governed by the temperature-dependent Cauchy equation, derived from Eqs. (1) and (2):

$$-\rho_0 \omega^2 \mathbf{u}_1^d = \nabla \cdot \boldsymbol{\sigma}_1^{\text{sl},d}, \quad (26a)$$

$$\boldsymbol{\sigma}_1^{\text{sl},d} = -\frac{\alpha_p}{\kappa_T} T_1^d \mathbf{I} + \boldsymbol{\tau}_1, \quad (26b)$$

$$\boldsymbol{\tau}_1^{\text{sl},d} = \rho_0 c_{\text{tr}}^2 [\nabla \mathbf{u}_1 + (\nabla \mathbf{u}_1)^T] + \rho_0 (c_{\text{lo}}^2 - 2c_{\text{tr}}^2) (\nabla \cdot \mathbf{u}_1) \mathbf{I}. \quad (26c)$$

The boundary layers at the fluid-solid interface are incorporated analytically through two effective boundary conditions.

First [see Ref. [7], Eq. (34a)], the velocity must be continuous across the interface, here imposed on $\partial_z p_1$ in the fluid,

$$\begin{aligned} \partial_z p_1 = i \frac{\omega \rho_0}{1 - i\Gamma_s} \left(V_{1z}^0 - \frac{i}{k_s} \nabla \cdot \mathbf{V}_1^0 \right) - \frac{i}{k_s} (k_c^2 + \partial_z^2) p_1 \\ + \frac{i}{k_t} \frac{\alpha_p}{\kappa_T} k_0^2 T_1^{\text{fl},\delta 0}, \quad \text{for } z = 0, \end{aligned} \quad (27a)$$

where $T_1^{\text{fl},\delta 0}$ is the boundary-layer temperature field given in the following subsection. Second [see Ref. [7], Eq. (34b)], the stress must be continuous across the interface, here imposed on $\boldsymbol{\sigma}_1^{d,\text{sl}}$ in the solid,

$$\boldsymbol{\sigma}_1^{\text{sl},d} \cdot \mathbf{e}_z = -p_1 \mathbf{e}_z + ik_s \eta_0 \left(\mathbf{v}_1^{\text{sl},d0} + \frac{i}{\omega \rho_0} \nabla p_1 \right). \quad (27b)$$

The effective boundary conditions (27) enable 3D simulations with a coarse mesh, because the boundary layer does not need to be resolved numerically.

B. Analytical form of the boundary layers

The analytical solution for the boundary layers was in Ref. [7] used to set effective boundary conditions on the acoustic fields and the steady streaming field. Here we also need them to derive the effective boundary conditions for the steady temperature field. The analytical solution of the temperature boundary layer in the fluid $T_1^{\text{fl},\delta}$ and solid $T_1^{\text{sl},\delta}$ is given in Ref. [7] Eq. (29) as

$$T_1^{\text{fl},\delta} = -\frac{\tilde{Z}}{1 + \tilde{Z}} [T_1^{\text{sl},d0}(x, y) - T_1^{\text{fl},d0}(x, y)] e^{ik_t^{\text{fl}} z}, \quad (28a)$$

$$T_1^{\text{sl},\delta} = +\frac{1}{1 + \tilde{Z}} [T_1^{\text{sl},d0}(x, y) - T_1^{\text{fl},d0}(x, y)] e^{-ik_t^{\text{sl}} z}, \quad (28b)$$

$$\tilde{Z} = \frac{k_0^{\text{th,sl}} k_t^{\text{sl}}}{k_0^{\text{th,fl}} k_t^{\text{fl}}} = \sqrt{\frac{k_0^{\text{th,sl}} c_{p0}^{\text{sl}} \rho_0^{\text{sl}}}{k_0^{\text{th,fl}} c_{p0}^{\text{fl}} \rho_0^{\text{fl}}}}. \quad (28c)$$

Here, the superscript “xl, d0” refers to fluid (xl = fl) or solid (xl = sl), and to a bulk field (d) on the boundary (0) that depends only on the local in-plane coordinates (x, y) and not on the local perpendicular coordinate z .

The acoustic velocity \mathbf{v}_1 is split into three fields [see Ref. [7], Eqs. (20a)]: the bulk velocity $\mathbf{v}_1^{d,p}$ and the thermal boundary-layer velocity $\mathbf{v}_1^{d,T}$, both compressible gradient fields in the Helmholtz decomposition (superscript d), as well as the viscous boundary-layer velocity \mathbf{v}_1^δ ,

$$\mathbf{v}_1 = \mathbf{v}_1^{d,p} + \mathbf{v}_1^{d,T} + \mathbf{v}_1^\delta. \quad (29)$$

As derived analytically in Ref. [7], Eqs. (30) and (33b), \mathbf{v}_1^δ and $\mathbf{v}_1^{d,T}$ are given by

$$\mathbf{v}_1^\delta = \mathbf{v}_1^{\delta 0}(x, y) e^{ik_s z}, \quad (30a)$$

$$\mathbf{v}_1^{d,T} = \alpha_{p0} D_0^{\text{th}} \nabla T_1^\delta = \frac{\alpha_{p0} k_0^{\text{th}}}{\rho_0 c_{p0}} \nabla T_1^\delta. \quad (30b)$$

These analytical expressions are used in Sec. IV C to derive the contribution from the acoustic fields to the boundary condition of the steady thermal field.

In terms of bulk and boundary fields combined with Eqs. (6b) and (7a), the first-order density ρ_1 , viscosity η_1 , and thermal conductivity k_1^{th} are written as

$$\rho_1 = \rho_1^d + \rho_1^\delta, \quad \rho_1^\delta = -\rho_0 \alpha_p T_1^\delta, \quad \rho_1^d = \rho_0 \kappa_s p_1, \quad (31a)$$

$$\eta_1 = \eta_1^d + \eta_1^\delta, \quad \eta_1^\delta = \eta_0 a_\eta^T \alpha_p T_1^\delta, \quad \eta_1^d = \eta_0 a_\eta^{p,\text{ad}} \kappa_s p_1, \quad (31b)$$

$$k_1^{\text{th}} = k_1^{\text{th},d} + k_1^{\text{th},\delta}, \quad k_1^{\text{th},\delta} = k_0^{\text{th}} a_{k^{\text{th}}}^T \alpha_p T_1^\delta, \quad k_1^{\text{th},d} = k_0^{\text{th}} a_{k^{\text{th}}}^{p,\text{ad}} \kappa_s p_1. \quad (31c)$$

IV. STEADY FIELDS

The steady part of thermoviscous acoustofluidics contains mechanical and temperature fields. The mechanical fields are studied in Ref. [7], so the equations for the displacement \mathbf{u}_0 in the solid and pressure p_0 and velocity \mathbf{v}_0 in the fluid, can be carried over unchanged, and we just summarize the main results below. However, we need to develop the theory for the steady temperature field T_0 , both its bulk part T_0^d and its boundary-layer part T_0^δ , as it is not treated in Ref. [7].

A. Mechanical bulk and boundary-layer fields

As $|\mathbf{u}_0| \ll \delta \ll d$, the steady displacement field \mathbf{u}_0 is decoupled from both the steady thermal field and the acoustic fields, and consequently

$$\mathbf{u}_0 = \mathbf{0}. \quad (32)$$

The steady pressure p_0 and streaming \mathbf{v}_0 are governed by the steady part of Eqs. (4a) and (4b),

$$0 = \nabla \cdot \mathbf{v}_0^d, \quad (33a)$$

$$0 = -\nabla [p_0^d - \mathcal{L}_{\text{ac}}^d] - \nabla \cdot [\rho_0 \mathbf{v}_0 \mathbf{v}_0] + \eta_0 \nabla^2 \mathbf{v}_0^d + \mathbf{f}_{\text{ac}}^d. \quad (33b)$$

Here the time-averaged Lagrangian density $\mathcal{L}_{\text{ac}}^d$ and acoustic body force \mathbf{f}_{ac}^d are given by Ref. [7], Eq. (52c),

$$\mathcal{L}_{\text{ac}}^d = \frac{1}{4} \kappa_s |p_1|^2 - \frac{1}{4} \rho_0 |\mathbf{v}_1^{d,p}|^2, \quad (34a)$$

$$\begin{aligned} \mathbf{f}_{\text{ac}}^d = & -\frac{1}{4} |\mathbf{v}_1^{d,p}|^2 \nabla \rho_0 - \frac{1}{4} |p_1|^2 \nabla \kappa_s \\ & + \left[1 - \frac{2a_\eta(\gamma - 1)}{\beta + 1} \right] \frac{\Gamma \omega}{c^2} \langle \mathbf{v}_1^{d,p} p_1 \rangle \\ & + a_\eta \eta_0 (\gamma - 1) k_c^2 \langle \mathbf{s}_1^d \cdot \nabla \mathbf{v}_1^{d,p} \rangle. \end{aligned} \quad (34b)$$

The acoustic boundary layers, are taken into account analytically, and they only appear implicitly by imposing a slip velocity \mathbf{v}_0^{d0} on the bulk streaming field \mathbf{v}_0^d given by Ref. [7] Eq. (54) as $\mathbf{v}_0^d(s_o) = \mathbf{v}_0^{d0}$, with

$$\mathbf{v}_0^{d0} = (\mathbf{A} \cdot \mathbf{e}_x) \mathbf{e}_x + (\mathbf{A} \cdot \mathbf{e}_y) \mathbf{e}_y + (\mathbf{B} \cdot \mathbf{e}_z) \mathbf{e}_z, \quad (35a)$$

$$\mathbf{A} = -\frac{1}{2\omega} \text{Re} \left\{ \mathbf{v}_1^{\delta 0*} \cdot \nabla \left(\frac{1}{2} \mathbf{v}_1^{\delta 0} - i \mathbf{V}_1^{0*} \right) - i \mathbf{V}_1^{0*} \cdot \nabla \mathbf{v}_1^{d,p} \right.$$

$$\left. + \left[\frac{2-i}{2} \nabla \cdot \mathbf{v}_1^{\delta 0*} + i \left(\nabla \cdot \mathbf{V}_1^{0*} - \partial_z v_{1z}^{d*} \right) \right] \mathbf{v}_1^{\delta 0} \right\} + \frac{1}{2\eta_0} \text{Re} \left(\eta_1^{d0} \mathbf{v}_1^{\delta 0*} + \frac{\delta_t}{\delta_t - i\delta_s} \eta_1^{\delta 0} \mathbf{v}_1^{\delta 0*} \right), \quad (35b)$$

$$\mathbf{B} = \frac{1}{2\omega} \text{Re} (i \mathbf{v}_1^{d0*} \cdot \nabla \mathbf{v}_1^{d,p}), \quad (35c)$$

$$\mathbf{v}_1^{\delta 0} = -i\omega \mathbf{u}_1^0 - \mathbf{v}_1^{d0}, \quad (35d)$$

$$\eta_1^{\delta 0} = -\frac{\tilde{Z}}{1 + \tilde{Z}} \eta_0 a_\eta^T \alpha_p (T_1^{\text{sl},d0} - T_1^{\text{fl},d0}), \quad (35e)$$

$$\eta_1^{d0} = \eta_0 a_\eta^{p,\text{ad}} \kappa_s p_1, \quad (35f)$$

where the expressions for $\mathbf{v}_1^{\delta 0}$, $\eta_1^{\delta 0}$, and η_1^{d0} in terms of bulk fields are obtained from Eqs. (16), (28a), and (31b).

B. Steady temperature fields

The steady temperature field T_0 is given as the time-averaged terms of Eqs. (1b) and (4c) in the solid and fluid, respectively. The time averaged terms either consist of steady fields a_0 or terms with time-averaged products $\langle a_1 b_1 \rangle$ of two acoustic fields a_1 and b_1 . All terms of the latter type are collected as an acoustic power P_{ac} . In the fluid, neglecting small terms by using $\mathbf{v}_0 \cdot \boldsymbol{\sigma}_{11} \ll \langle \mathbf{v}_1 \cdot \boldsymbol{\sigma}_1 \rangle$, $\rho_1 \mathbf{v}_0 \ll \rho_0 \mathbf{v}_1$, $\nabla \cdot \langle \rho_0 \mathbf{v}_0 + \rho_1 \mathbf{v}_1 \rangle = 0$, $\epsilon_{11} + \frac{1}{2} |\mathbf{v}_0|^2 + \frac{1}{2} |\mathbf{v}_1|^2 \ll \epsilon_0$, $\epsilon_1^d = c_{p0} T_1^d - \frac{\alpha_{p0} T_0}{\rho_0} p_1^d = 0$, $\epsilon_1^\delta = c_{p0} T_1^\delta$, and $|\mathbf{v}_0 \cdot \boldsymbol{\sigma}_0| \ll |k_0^{\text{th}} \nabla T_0|$, the steady part of Eq. (4c) becomes

$$0 = \nabla \cdot (k_0^{\text{th}} \nabla T_0^{\text{fl}}) - c_p \rho_0 \mathbf{v}_0 \cdot \nabla T_0^{\text{fl}} + P_{\text{ac}}^{\text{fl}} + P, \quad (36a)$$

$$\begin{aligned} P_{\text{ac}}^{\text{fl}} = & \nabla \cdot \left(\langle k_1^{\text{th}} \nabla T_1^{\text{fl}} \rangle - \langle p_1 \mathbf{v}_1 \rangle + \langle \mathbf{v}_1 \cdot \boldsymbol{\tau}_1 \rangle \right. \\ & \left. - \rho_0 c_{p0} \langle T_1^{\text{fl}} \mathbf{v}_1 \rangle \right) - c_p \langle \rho_1 \mathbf{v}_1 \rangle \cdot \nabla T_0^{\text{fl}}. \end{aligned} \quad (36b)$$

In the solid there is no advection, and the T_0 part of Eq. (1b) is controlled by thermal diffusion alone,

$$0 = \nabla \cdot (k_0^{\text{th}} \nabla T_0^{\text{sl}}) + P_{\text{ac}}^{\text{sl}} + P, \quad (37a)$$

$$P_{\text{ac}}^{\text{sl}} = \nabla \cdot \langle k_1^{\text{th}} \nabla T_1^{\text{sl}} \rangle. \quad (37b)$$

In both the solid (sl) and the fluid (fl), the steady temperature field and the time-averaged acoustic power are separated into a bulk (d) and a boundary (δ) term,

$$T_0^{\text{xl}} = T_0^{\text{xl},d} + T_0^{\text{xl},\delta}, \quad P_{\text{ac}} = P_{\text{ac}}^d + P_{\text{ac}}^\delta. \quad (38)$$

The boundary-layer temperature fields $T_0^{\text{fl},\delta}$ and $T_0^{\text{sl},\delta}$ are defined as the response to P_{ac}^δ , and all three fields are required to go to zero far away from the boundary.

The two bulk and two boundary-layer fields are linked by the boundary conditions (19a) and (21a) at the fluid-solid interface, which impose continuity of the temperature and of the heat flux density. The first is

$$T_0^{\text{fl},d0} + T_0^{\text{fl},\delta 0} + \langle \mathbf{s}_1 \cdot \nabla T_1^{\text{fl}} \rangle = T_0^{\text{sl},d0} + T_0^{\text{sl},\delta 0}, \quad (39a)$$

and the second is

$$\begin{aligned} k_0^{\text{th}} \mathbf{n} \cdot \nabla (T_0^{\text{fl},d} + T_0^{\text{fl},\delta}) + \langle k_1^{\text{th}} \mathbf{n} \cdot \nabla T_1^{\text{fl}} \rangle + \langle \mathbf{s}_1 \cdot \nabla (k_0^{\text{th}} \nabla T_1^{\text{fl}}) \cdot \mathbf{n} \rangle \\ = -k_0^{\text{th},\text{sl}} \mathbf{n} \cdot \nabla (T_0^{\text{sl},d} + T_0^{\text{sl},\delta}) - \langle k_1^{\text{th},\text{sl}} \mathbf{n} \cdot \nabla T_1^{\text{sl}} \rangle. \end{aligned} \quad (39b)$$

Thus, the steady bulk solid and fluid fields $T_0^{\text{sl},d}$ and $T_0^{\text{fl},d}$ can be matched at the interface by using the analytical form of the boundary-layer fields $T_0^{\text{sl},\delta}$ and $T_0^{\text{fl},\delta}$.

C. Steady boundary-layer temperature fields

In the fluid, the boundary-layer $T_1^{\text{fl},\delta}$ is driven by P_{ac}^δ of Eqs. (36b) and (38). We neglect the convection term $c_{p0}(\rho_0 \mathbf{v}_0 + \langle \rho_1 \mathbf{v}_1 \rangle) \nabla T$ in the boundary layer, because it contains only one gradient $\propto \delta^{-1}$ and thus is a factor $k\delta$ smaller than the viscous term $\nabla \cdot \langle \mathbf{v}_1 \cdot \boldsymbol{\tau}_1 \rangle$ containing two gradients $\propto \delta^{-2}$. Moreover, in the boundary layer we have $\nabla \cdot [k_0^{\text{th}} \nabla T_0^{\text{fl},\delta}] \approx k_0^{\text{th}} \partial_z^2 T_0^\delta$, so the governing equation for the steady boundary-layer temperature field $T_0^{\text{fl},\delta}$ therefore reduces to

$$\begin{aligned} k_0^{\text{th}} \partial_z^2 T_0^{\text{fl},\delta} &= -P_{\text{ac}}^\delta \quad (40a) \\ P_{\text{ac}}^\delta &= \nabla \cdot (\langle k_1^{\text{th}} \nabla T_1 \rangle^{\text{fl},\delta} + \langle \mathbf{v}_1 \cdot \boldsymbol{\tau}_1 \rangle^{\text{fl},\delta} \\ &\quad - \langle p_1 \mathbf{v}_1 \rangle^{\text{fl},\delta} - \rho_0 c_{p0} \langle T_1 \mathbf{v}_1 \rangle^{\text{fl},\delta}). \quad (40b) \end{aligned}$$

The notation $\langle \dots \rangle^\delta$ denotes all the terms that contain at least one boundary-layer term T_1^δ or \mathbf{v}_1^δ . The first-order boundary-layer fields are known analytically (see Sec. III B), so we can evaluate the four terms in P_{ac}^δ . We integrate Eq. (40a) once from $z = \infty$ to $z = 0$ to find the normal derivative $\partial_z T_0^{\text{fl},\delta}$, and twice to find the value $T_0^{\text{fl},\delta}$. We describe each field at $z = 0$ as a surface field (with superscript “0”), which depends only on x and y , multiplied by the exponential z dependence given analytically in Sec. III B. The reduction and integration of the four terms is straightforward but tedious as shown in Appendix A. The normal gradient $\partial_z T_0^{\text{fl},\delta}$ at the fluid-solid interface becomes [Eq. (A13)]

$$\begin{aligned} \partial_z T_0^{\text{fl},\delta 0} &= \text{Re} \left(\frac{1+i}{4D_0^{\text{th}}} \left\{ \frac{1-i}{2} \frac{\delta_s \omega}{c_p} \mathbf{v}_1^{\delta 0} \cdot \mathbf{v}_1^{\delta 0*} - \frac{\delta_t \omega \alpha_{p0}}{c_p \rho_0} p_1^0 T_1^{\delta 0*} \right. \right. \\ &\quad - \frac{\delta_s}{\delta_s + i\delta_t} [\delta_t \nabla_{\parallel} T_1^{\delta 0} \cdot \mathbf{v}_1^{\delta 0*} - (1-i) T_1^{\delta 0} v_{1,z}^{\delta 0*}] \\ &\quad - iT_1^{\delta 0} [v_{1,z}^{d,T0*} + (1+i)v_{1,z}^{d,p0*} - \delta_t \omega \kappa_s p_1^{0*}] \\ &\quad \left. \left. - \delta_t \nabla_{\parallel} T_1^{\delta 0} \cdot \mathbf{v}_1^{d,p0*} + \delta_t \omega \frac{k_1^{\text{th},\delta 0} + k_1^{\text{th},d0}}{k_0^{\text{th}}} T_1^{\delta 0*} \right\} \right), \quad (41a) \end{aligned}$$

where all quantities are evaluated in the fluid. The boundary-layer heat flux $k_0^{\text{th},\text{fl}} \partial_z T_0^{\text{fl},\delta 0}$ is dominated by the first term $\mathbf{v}_1^{\delta 0} \cdot \mathbf{v}_1^{\delta 0*}$ which is a factor of $\alpha_{p0} T_0 \simeq 10$ larger than the terms including the boundary layer temperature field $T_1^{\delta 0}$. The two last terms including k_1^{th} are smaller by a factor of $\gamma - 1$ and are therefore important only for gases and not liquids. The result Eq. (A15) for the boundary-layer interface temperature $T_0^{\text{fl},\delta 0}$ is

$$\begin{aligned} T_0^{\text{fl},\delta 0} &= \frac{\delta_t}{4D_0^{\text{th}}} \text{Re} \left\{ -\frac{\delta_s^2 \omega}{2\delta_t c_p} \mathbf{v}_1^{\delta 0} \cdot \mathbf{v}_1^{\delta 0*} + \frac{\delta_t \omega \alpha_{p0}}{c_p \rho_0} p_1^0 T_1^{\delta 0*} \right. \\ &\quad \left. + i \frac{\delta_s^2}{(\delta_s + i\delta_t)^2} [\delta_t \nabla_{\parallel} T_1^{\delta 0} \cdot \mathbf{v}_1^{\delta 0*} - (1-i) T_1^{\delta 0} v_{1,z}^{\delta 0*}] \right\} \end{aligned}$$

$$\begin{aligned} &- T_1^{\delta 0} \left[\frac{1-i}{2} v_{1,z}^{d,T0*} + (1+i)v_{1,z}^{d,p0*} - \delta_t \omega \kappa_s p_1^{0*} \right] \\ &+ i\delta_t \nabla_{\parallel} T_1^{\delta 0} \cdot \mathbf{v}_1^{d,p0*} - \delta_t \omega \frac{(1+i)k_1^{\text{th},\delta 0} + 2k_1^{\text{th},d0}}{2k_0^{\text{th}}} T_1^{\delta 0*} \}. \quad (41b) \end{aligned}$$

Again, the first term $\mathbf{v}_1^{\delta 0} \cdot \mathbf{v}_1^{\delta 0*}$ originating from the viscous boundary layer is the leading term.

In the solid, the boundary layer field $T_0^{\text{sl},\delta}$ is governed by P_{ac}^δ of Eqs. (37b) and (38) as

$$0 = -\nabla \cdot (k_0^{\text{th},\text{sl}} \nabla T_0^{\text{sl},\delta} + \langle k_1^{\text{th},\text{sl}} \nabla T_1^{\text{sl}} \rangle^\delta), \quad (42)$$

which, when using $\nabla^2 T_0^{\text{sl},\delta} \simeq \partial_z^2 T_0^{\text{sl},\delta}$, gives the following differential equation for the boundary-layer field $T_0^{\text{sl},\delta}$:

$$k_0^{\text{th},\text{sl}} \partial_z^2 T_0^{\text{sl},\delta} = -\nabla \cdot \langle k_1^{\text{th},\text{sl}} \nabla T_1^{\text{sl}} \rangle^\delta. \quad (43)$$

The right-hand side is similar to $\nabla \cdot \langle k_1^{\text{th}} \nabla T_1^{\text{fl}} \rangle^\delta$ in the fluid boundary layer, which contributes with terms of the type $k_1^{\text{th}} T_1^{\delta 0*}$ in Eqs. (41a) and (41b). These terms in the fluid domain can be directly transferred to the solid domain, which results in the following normal heat flux and temperature in the boundary layer on the solid side of the fluid-solid interface:

$$\partial_z T_0^{\text{sl},\delta} = \frac{1}{2\delta_t} \text{Re} \left[(1+i) \frac{k_1^{\text{th},\delta 0} + k_1^{\text{th},d0}}{k_0^{\text{th}}} T_1^{\delta 0*} \right], \quad (44a)$$

$$T_0^{\text{sl},\delta} = -\frac{1}{4} \text{Re} \left[\frac{(1+i)k_1^{\text{th},\delta 0} + 2k_1^{\text{th},d0}}{k_0^{\text{th}}} T_1^{\delta 0*} \right], \quad (44b)$$

where all quantities are evaluated in the solid. For a fluid-solid interface these terms are negligible compared to the leading term in the fluid boundary layer. They can be important for certain gas-solid interfaces.

D. Steady bulk temperature fields

The steady bulk temperature field $T_0^{\text{fl},d}$ in the fluid is governed by the long-range bulk terms of Eq. (36),

$$\begin{aligned} 0 &= \nabla \cdot (k_0^{\text{th}} \nabla T_0^{\text{fl},d}) - c_p \rho_0 \mathbf{v}_0 \cdot \nabla T_0^{\text{fl},d} + P_{\text{ac}}^d + P, \quad (45a) \\ P_{\text{ac}}^d &= \nabla \cdot (\langle k_1^{\text{th},d} \nabla T_1^d \rangle - \langle p_1 \mathbf{v}_1^{d,p} \rangle + \langle \mathbf{v}_1^{d,p} \cdot \boldsymbol{\tau}_1^d \rangle) \\ &\quad - c_p \langle \rho_1^d \mathbf{v}_1^{d,p} \rangle \cdot \nabla T_0^d. \quad (45b) \end{aligned}$$

Similarly, $T_0^{\text{sl},d}$ in the solid is governed by the long-range bulk terms of Eq. (37),

$$0 = \nabla \cdot (k_0^{\text{th}} \nabla T_0^{\text{sl},d}) + P_{\text{ac}}^d + P, \quad (46a)$$

$$P_{\text{ac}}^d = \nabla \cdot \langle k_1^{\text{th},\text{sl}} \nabla T_1^{\text{sl},d} \rangle. \quad (46b)$$

Here P is an external heat power source from fields not included in the model, such as heat generated by light absorption or by Joule heating from electric currents. The bulk fields $T_0^{\text{sl},d}$ and $T_0^{\text{fl},d}$ are connected at the fluid-solid interface by the

Dirichlet and Neumann boundary conditions (39a) and (39b).

We choose to apply the Dirichlet condition (39a) on $T_0^{\text{fl},d}$ in the fluid and therefore write

$$T_0^{\text{fl},d} = T_0^{\text{sl},d} - T_0^{\text{fl},\delta 0} - \frac{1}{2} \text{Re} [s_1 \cdot \nabla T_1^{\text{fl},d*} - k_t^{\text{fl}}(s_1 \cdot \mathbf{n}) T_1^{\text{fl},\delta 0*}]. \quad (47)$$

All fields on the right-hand side can be expressed in terms of bulk fields: the acoustic boundary-layer fields $T_1^{\text{fl},\delta}$ and $T_1^{\text{sl},\delta}$ through $T_1^{\text{fl},d}$ and $T_1^{\text{sl},d}$ by Eq. (28), the steady boundary-layer fields $T_0^{\text{fl},\delta}$ and $T_0^{\text{sl},\delta}$ through $T_1^{\text{fl},\delta}$, $T_1^{\text{sl},\delta}$, $T_1^{\text{fl},d}$, $T_1^{\text{sl},d}$, and p_1 by Eqs. (31), (41b), and (44b), and finally s_1 through \mathbf{u}_1 by the simple identification $s_1 = \mathbf{u}_1(s_0)$. Consequently, $T_0^{\text{fl},d}$ is given solely by steady and acoustic bulk fields, a crucial point in the implementation of a numerical simulation involving only bulk fields, which avoids the numerically demanding resolution of the narrow boundary layers. Note how the boundary-layer fields result in a discontinuity in the bulk temperature across the fluid-solid interface; see Fig. 1(b).

Conversely, the Neumann boundary condition (39b) is enforced on the temperature field $T_0^{\text{sl},d}$ in the solid. Together with the evaluation of the steady boundary layer terms in Eqs. (41a) and (44), it becomes

$$k_0^{\text{th,sl}} \mathbf{n} \cdot \nabla T_0^{\text{sl},d} = k_0^{\text{th,fl}} \mathbf{n} \cdot \nabla T_0^{\text{fl},d} + k_0^{\text{th,fl}} \partial_z T_0^{\text{fl},\delta} + \frac{1}{2} \text{Re} \left[k_t^{\text{fl}} k_1^{\text{th,fl}} T_1^{\text{fl},\delta*} - \frac{2i}{\delta_l^2} k_0^{\text{th,fl}} (s_1 \cdot \mathbf{n}) T_1^{\text{fl},\delta*} \right]. \quad (48)$$

Similar to Eq. (47), all fields on the right-hand side of Eq. (48) can be expressed in terms of steady and acoustic bulk fields through $T_1^{\text{fl},\delta}$, $T_1^{\text{sl},\delta}$, $T_1^{\text{fl},d}$, $T_1^{\text{sl},d}$, and p_1 by Eqs. (31), (41a), and (44a), and by using $s_1 = \mathbf{u}_1(s_0)$. Consequently, $\partial_z T_0^{\text{fl},d}$ is given solely by steady and acoustic bulk fields.

In summary, the bulk temperature fields are governed by Eqs. (45) and (46) together with the effective boundary conditions (47) and (48), in which the boundary-layer fields are taken into account analytically and expressed in terms of bulk fields. The boundary conditions on the outer surfaces could either be a Dirichlet boundary condition, such as Peltier elements or heat sinks, a no-flux boundary condition as for an air interface, or a combination such as air cooling and solids made of glass or polymer with a thermal diffusivity similar to water.

V. AN ITERATIVE PROCEDURE TO ACCOUNT FOR NONLINEAR EFFECTS

The separation of timescales leaves us with one set of equations presented in Sec. III for the acoustic fields p_1 and \mathbf{u}_1 , and another set presented in Sec. IV for the steady fields \mathbf{v}_0 , p_0 , T_0^{sl} , and T_0^{fl} . These steady and acoustic fields impact each other through the temperature-dependent material parameters, the acoustic body force \mathbf{f}_{ac}^d , the acoustic power P_{ac} , and the effective boundary conditions, in which the boundary-layer fields are taken into account analytically but appear only implicitly through expressions involving only bulk fields. As described in the following, the combined set of equations can be solved by a self-consistent iterative procedure, in which the

coupled acoustic and steady fields are solved in an iterative sequence until convergence is obtained.

The steady fields \mathbf{v}_0 , p_0 , T_0^{sl} , and T_0^{fl} are computed from the governing equations (33), (45), and (46) in the bulk with the effective boundary conditions (35), (47), and (48). The acoustic fields p_1 and \mathbf{u}_1 are computed from the governing equations (25) and (26) with the effective boundary conditions (27).

The equations are implemented in COMSOL Multiphysics [28] using the Weak Form PDE Interface, and the effective boundary conditions are set using the Dirichlet Boundary Condition Interface (Eq. (3) for the actuation $\mathbf{u}_1 = \mathbf{u}_{\text{exc}}$, Eq. (35) for the slip velocity $\mathbf{v}_0^d = \mathbf{v}_0^{d0}$, and Eq. (47) for the temperature $T_0^{\text{fl},d}$ in the fluid) and the Weak Contribution Interface [Eq. (27) for the pressure gradient $\partial_z p_1$ and the stress $\boldsymbol{\sigma}_1^{\text{sl},d}$, and Eq. (48) for the heat flux $k_0^{\text{th,sl}} \mathbf{n} \cdot \nabla T_0^{\text{sl},d}$ on the solid]. The iterative solver is implemented using the Segregated Solver with two steps: Step 1 computes the steady fields \mathbf{v}_0 , p_0 , T_0^{sl} , and T_0^{fl} based on the current value of the acoustic fields, and Step 2 computes the acoustic fields \mathbf{u}_1 and p_1 based on the current value of the steady fields. The segregated solver then runs until convergence is obtained.

The benefit of the iterative setup compared to the traditional perturbation setup [1,5–7] is that nonperturbative effects are included. In the steady fields there are two dominating nonperturbative effects in typical microscale acoustofluidic devices: (1) Thermal convection proportional to $\mathbf{v}_0 \cdot \nabla T_0$, which dominates over thermal diffusion proportional to $\nabla^2 T_0$, when $|\mathbf{v}_0| \gtrsim D_0^{\text{th}}/d \approx 0.3\text{--}1.5$ mm/s for $d = 100\text{--}500$ μm . Note that for larger systems convection becomes important at lower velocities. This limit is easily reached in typical experiments [8]. (2) Acoustic heating, which is due to the viscous dissipation P_{ac}^{δ} in the viscous boundary layer, and which may lead to temperature gradients in the bulk large enough to result in a significant acoustic body force proportional to $|p_1|^2 \nabla T_0$ through the temperature-dependent compressibility and density [see Eq. (34b)] that drive an acoustic streaming, which at sufficiently high acoustic energy densities dominates over the usual boundary-driven Rayleigh streaming.

The thermal convection will become important when the thermal Péclet number $\text{Pe} = |\mathbf{v}_0|d/D_0^{\text{th}}$ is similar to unity, which occurs at $|\mathbf{v}_0| \sim D_0^{\text{th}}/d$. For water in a system with a characteristic length $d = 0.5$ mm, the convective flow is important at $|\mathbf{v}_0| \geq 300$ $\mu\text{m/s}$. The inhomogeneous acoustic body force due to acoustic heating is important to include, when it is dominant compared to the traditional Eckart streaming,

$$\frac{1}{4} |p_1|^2 |\nabla \kappa_T(T_0)| \gtrsim \frac{\Gamma \omega}{c_0^2} |(\mathbf{v}_1^d p_1)|. \quad (49)$$

By using $|\mathbf{v}_1| \approx \frac{1}{\omega \rho_0} k_0 |p_1|$, $\nabla T_0 = d^{-1} \Delta T_0$, and the thermal dependency of the compressibility a_{κ}^T . Here d is the length scale over which the temperature field varies with ΔT_0 , this will typically be determined by the geometry. Then the thermoacoustic term is dominant when

$$\Delta T_0 \gtrsim \frac{4\Gamma k_0 d}{\alpha_p a_{\kappa_s}}. \quad (50)$$

TABLE I. Physical parameters at 25 °C of the materials water, rapeseed oil, glass, and silicon used in the examples.

Parameter	Symbol	Unit	Water [2]	Rapeseed oil [35]	Glass	Silicon
Mass density	ρ	kg m ⁻³	997	924	2230	2329
Thermal conductivity	k^{th}	W m ⁻¹ K ⁻¹	0.61	0.17	1.14	149
Specific heat capacity	c_p	J kg ⁻¹ K ⁻¹	4181	2197	800	750
Thermal expansion coefficient	α_p	K ⁻¹	2.57×10^{-4}	6.61×10^{-4}	–	–
Ratio of specific heat capacity	γ	–	1.011	1.0105	–	–
Longitudinal sound speed	c_{10}	m s ⁻¹	1497	1451	5600	8440
Transverse sound speed	c_{tr}	m s ⁻¹	–	–	3350	5860
Sound speed, cubic symmetry	c_{12}	m s ⁻¹	–	–	–	5360
Shear viscosity	η	Pa s	8.9×10^{-4}	0.047	–	–
Bulk viscosity	η^{b}	Pa s	2.485×10^{-3}	0.17	–	–
Compressibility	κ_T	Pa ⁻¹	4.52×10^{-10}	5.14×10^{-10}	–	–
Thermal derivative of κ_s	$\partial_T \kappa_s$	Pa ⁻¹ K ⁻¹	-1.12	2.66	–	–

If $k_0 d \approx 1$ then the thermoacoustic streaming becomes important when $\Delta T_0 \approx 30$ mK. The lower bound for ΔT_0 in Eq. (50) is computed for water, using the values listed in Eq. (8).

VI. MODEL VALIDATION AND EXAMPLES

Below, we implement and validate our self-consistent iterative procedure in COMSOL Multiphysics 5.6 [28], and we study four specific examples of the mentioned nonperturbative effects, which our model is able to predict. All simulations are performed on a HP-G4 workstation with a processor Intel Core i9-7960X at 4:20 GHz and with 128 GB RAM.

A. Example in two dimensions: Change of the acoustic streaming due to internal acoustic heating

Our basic perturbative thermoviscous acoustofluidics model has previously been validated both numerically [7] and experimentally [8]. Therefore, we here choose our first example to be a 2D system, where we can validate numerically our iterative model with the effective boundary conditions (47) and (48) with a full iterative model, where the boundary layers are fully resolved. The chosen system is the rectangular

2D cross section of a long, straight water-filled microchannel embedded in a silicon base and capped with a glass lid, with the parameters listed in Table 1. In the literature, this system running with a horizontal acoustic half-wave resonance has been widely used to separate particles in a flow-through device and used in various studies both experimentally [16,17,19,36] and numerically [1,2]. Moreover, in Ref. [9], we have provided experimental validation of the iterative model presented below. The example aims to demonstrate three important points: (1) validation of the effective model, (2) modeling the internal acoustic heating in an acoustofluidic chip, and (3) demonstrating nonlinear effects at high acoustic energies beyond perturbation theory, effects that are further investigated by modeling and experiments in Ref. [9].

The model is a long straight silicon chip of width $W_{\text{Si}} = 3$ mm and height $H_{\text{Si}} = 0.4$ mm, inside which is placed a fluid channel of width $W = 375 \mu\text{m}$ and height $H = 135 \mu\text{m}$ and a capping Pyrex glass lid of height $H_{\text{Py}} = 1$ mm; see Fig. 2(a). Following Ref. [7], the actuation \mathbf{u}_{exc} on the bottom edge of the silicon chip is set to $\mathbf{u}_{\text{exc}} = \mathbf{u}_1^{\text{bot}}(\mathbf{y}) = \frac{2d_0}{W} y \mathbf{e}_z$ and the temperature to $T_0^{\text{bot}} = 25$ °C.

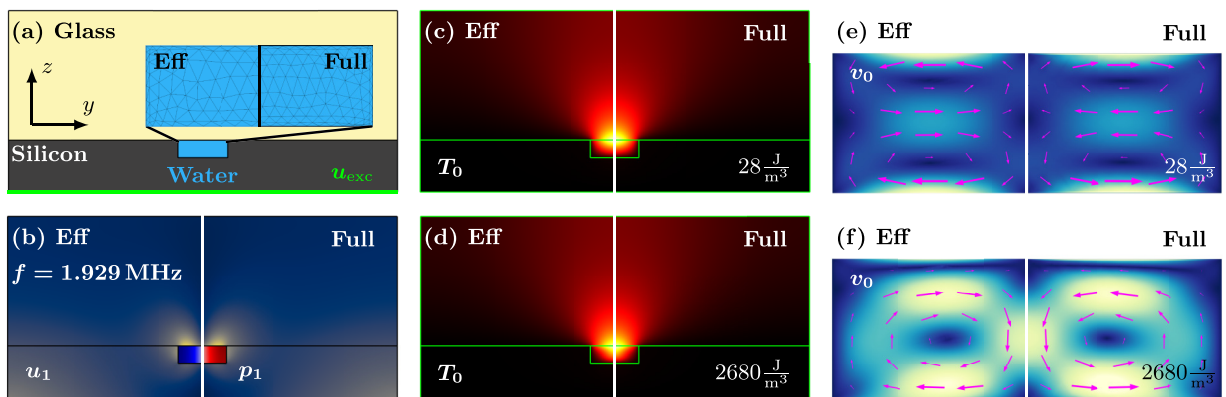


FIG. 2. Simulation of the effective (left, “Eff”) and the full model (right, “Full”) at the horizontal half-wave resonance $f = 1.929$ MHz. (a) The two-dimensional (2D) silicon-glass model with a water channel and the bottom-edge actuation \mathbf{u}_{exc} . (b) Color plot at the energy density $E_{\text{ac}} = 28 \text{ J/m}^3$ of the displacement $|\mathbf{u}_1|$ and pressure p_1 in the fluid. (c) Color plot at $E_{\text{ac}} = 28 \text{ J/m}^3$ of the steady temperature field $\Delta T_0 = T_0 - T_0^{\text{bot}}$ from 0 (black) to 8.7 mK (yellow). (d) Color plot at $E_{\text{ac}} = 2680 \text{ J/m}^3$ of ΔT_0 from 0 (black) to 230 mK (yellow). (e) Vector plot at $E_{\text{ac}} = 28 \text{ J/m}^3$ of the streaming \mathbf{v}_0 and color plot of its magnitude v_0 from 0 (blue) to 34 $\mu\text{m/s}$ (yellow). (f) Same as (e) but at $E_{\text{ac}} = 2680 \text{ J/m}^3$ and with v_0 from 0 (blue) to 4.0 mm/s (yellow).

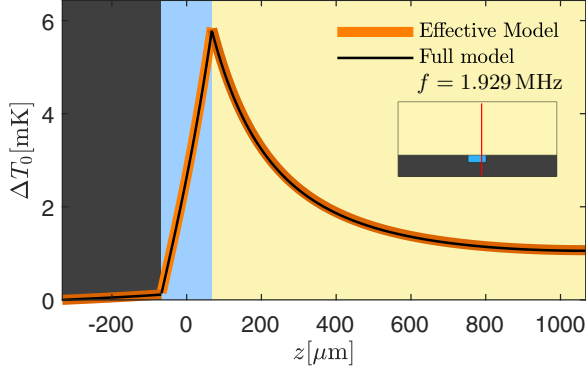


FIG. 3. Line plot at $E_{ac} = 28 \text{ J/m}^3$ and $f = 1.929 \text{ MHz}$ of the simulated steady temperature ΔT_0 in the effective and full model along the vertical red line $y = \frac{1}{4}W_n$ shown in the inset. The corresponding color plot of ΔT_0 is shown in Fig. 2(c).

In Fig. 2(a) is shown the coarse mesh of the effective model (422 elements) and the fine mesh (8362 elements) of the boundary-layer-resolving full model that are needed to fulfill a mesh-convergence criterium of an L_2 norm less than 1% [1] for the steaming velocity \mathbf{v}_0 at $E_{ac} = 28 \text{ J/m}^3$. For $E_{ac} = 28 \text{ J/m}^3$, the effective model takes 26 s and uses 2.1 GB RAM, whereas the full model takes 37 s and uses 5.1 GB RAM. The good agreement between the two models is shown in Figs. 2(b)–2(f) by the color plots of the resulting steady and acoustic fields computed from the effective (left side) and full (right side) model at a low (28 J/m^3) and a high (2680 J/m^3) acoustic energy density of E_{ac} . Moreover, the relative deviation between the two models in the computed values of the resonance frequency and Q factor of the 2 MHz half-wave resonance mode is less than 0.1%. Both models show how the well-known four-roll Rayleigh streaming pattern at the low E_{ac} changes into a two-roll pattern at high E_{ac} . In the perturbative model, p_1 , and \mathbf{u}_1 are linearly dependent on the actuation \mathbf{u}_{exc} , whereas T_0 , \mathbf{v}_0 , and $E_{ac} \propto d_0^2$. Hence, the spatial pattern of these fields is independent of \mathbf{u}_{exc} , but their respective amplitudes are proportional to the amplitude d_0 or d_0^2 . The perturbative model predicts that upon increasing E_{ac} from 28 to 2680 J/m^3 , the four-roll pattern of \mathbf{v}_0 in Fig. 2(e) should remain unchanged, but its amplitude change from 34 to 3.3 mm/s. Clearly, the iterative model result for \mathbf{v}_0 shown in Fig. 2(f) deviates both qualitatively and quantitatively from the perturbation prediction with its two-roll pattern with an amplitude of 4.0 mm/s, a clear display of the nonlinear effect arising from acoustic heating in the boundary layers. Note that the nonlinear effects from the heat convection is not strong enough to bring about a significant qualitative change in ΔT_0 increasing E_{ac} from 28 J/m^3 in Fig. 2(c) to 2680 J/m^3 in Fig. 2(d).

The effective boundary condition for the streaming velocity \mathbf{v}_0 was already validated in Ref. [7], so here we thus just need to validate the effective boundary conditions (45) and (46) on the steady temperature field T_0 . This is done in Fig. 3, showing excellent quantitative agreement between line plots of T_0 for the full and the effective model.

We end the example by discussing the physics that causes the difference from the linear case with four flow rolls to

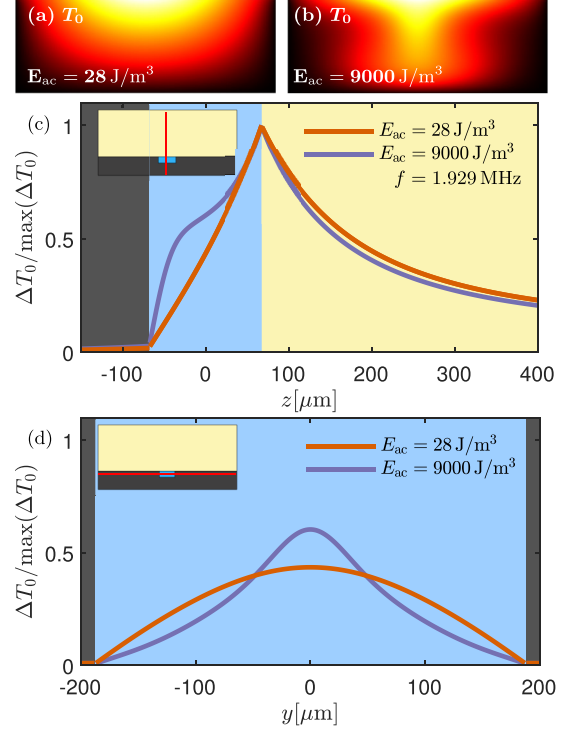


FIG. 4. (a) Color plot from 0 (black) to 8.7 mK (yellow) at $E_{ac} = 28 \text{ J/m}^3$ and $f = 1.929 \text{ MHz}$ of ΔT_0 from Fig. 2(c) zoomed in on the fluid domain. (b) Same as (a) but for $E_{ac} = 9000 \text{ J/m}^3$ and a color scale from 0 (black) to 2375 mK (yellow). (c) Line plot of the normalized temperature rise $\Delta T_0/\max(\Delta T_0)$ along the vertical line at $y = 0$ shown in the inset. (d) Same as (c) but along the horizontal line through the center of the microchannel shown in the inset.

the nonlinear case with two flow rolls. At the low acoustic energy density $E_{ac} = 28 \text{ J/m}^3$, the acoustic pressure p_1 and displacement \mathbf{u}_1 field as well as the steady temperature T_0 and streaming field \mathbf{v}_0 are shown in Figs. 2(b), 2(c), and 2(e). The source of the spatial inhomogeneities in T_0 in the fluid is the heat generation due to friction in the viscous boundary layer in the fluid at the top and bottom of the channel, and the different heat fluxes resulting from the relatively small values of the heat conductivity of water and glass compared to the large one of silicon. The latter ensures efficient transport of heat away from the bottom edge of the channel. Consequently, heating occurs only at the top of the channel near the glass lid, thus establishing a relatively large temperature gradient across the channel. In Figs. 4(a) and 4(b) the resulting temperature fields are shown for low (28 J/m^3) and high (9000 J/m^3) E_{ac} , respectively. In both cases, the temperature is clearly larger at the center of the top edge of the channel. However, for the high- E_{ac} case, the increased acoustic streaming is distorting the temperature field, as it induces a downward heat convection, which stretches the high-temperature region along a larger portion of the vertical center axis. The temperature boundary condition (47) results in nearly equal bulk and boundary layer temperature fields at the fluid-solid interface, $T_0^{fl,d0} \approx T_0^{fl,s0}$, so the gradients in the temperature field are governed by the effective boundary condition on the heat flux (48).

The streaming fields \mathbf{v}_0 for $E_{ac} = 28$ and 2680 J/m^3 are shown in Figs. 2(e) and 2(f), respectively. First, we see that the full and effective model result in the same \mathbf{v}_0 . Second, it is clear that at a low E_{ac} , the streaming is dominated by boundary-driven streaming, whereas at high E_{ac} , it is dominated by the bulk-driven streaming induced by the acoustic body force \mathbf{f}_{ac}^d of Eq. (34b). When gradients in density and compressibility are created by the temperature gradient, and the Eckart streaming is neglected, \mathbf{f}_{ac}^d becomes

$$\mathbf{f}_{ac}^d = -\frac{1}{4}(|p_1|^2 \partial_T \kappa_{s,0} + |\mathbf{v}_1|^2 \partial_T \rho_0) \nabla T_0. \quad (51)$$

The temperature gradient ∇T_0 and $|p_1|^2$ both scale with E_{ac} , so \mathbf{f}_{ac}^d , and thus the streaming scales with E_{ac}^2 . In comparison, the boundary-driven Rayleigh streaming scales with E_{ac} . Consequently, the bulk-driven streaming spawned by \mathbf{f}_{ac}^d will become dominant at sufficiently high E_{ac} . We study further this nonlinear behavior and transition both numerically and experimentally in Ref. [9].

Finally, we note that it is important that the device consists of a silicon base with a glass lid and not a pure glass chip, because the spatial asymmetry of T_0 , induced by the widely different thermal conductivities of the two materials, results in a skew-angled acoustic body force \mathbf{f}_{ac}^d that drives a strong thermoacoustic streaming \mathbf{v}_0 . The modeling of the transition into the nonlinear regime has not been captured by the previous perturbation models in the literature [2,5,7], because it requires a nonperturbative model that allows for E_{ac} -dependent spatial patterns of the fields as discussed in connection with Fig. 2.

B. Example in two dimensions: The influence of the thermal properties of the surrounding solid

The analysis of the silicon-glass system of Fig. 2 revealed, how the two-roll thermoacoustic streaming driven by the nonlinear acoustic body force \mathbf{f}_{ac}^d at high values of E_{ac} stems from the up-down asymmetry of T_0 due to the widely different thermal conductivities of the materials above and below the channel. To study this phenomenon further, we now strongly reduce the asymmetry of T_0 by substituting the silicon base by a glass base, leaving all other features unchanged, as sketched in Fig. 5(a). Here only the fixed temperature $T_0^{\text{bot}} = 25^\circ \text{C}$ of the heat sink at the bottom edge, breaks the up-down symmetry. Tuning the frequency to the horizontal half-wave resonance at 1.893 MHz [see p_1 in Fig. 5(b)], the spatial patterns in Figs. 5(c) and 5(e) of the temperature T_0 and the streaming \mathbf{v}_0 at $E_{ac} = 25 \text{ J/m}^3$ remain mainly unchanged, when increasing E_{ac} by a factor 80 to 2000 J/m^3 in Figs. 5(d) and 5(f). The field amplitudes are enhanced by the same factor 80, from 16 mK to 1.25 K for ΔT_0 and from $30 \mu\text{m/s}$ to 2.4 mm/s for \mathbf{v}_0 . Clearly this is the perturbation regime. T_0 is no longer confined to the water domain as in Figs. 2(c) and 2(d), but spreads out more evenly to the surrounding glass domain due to the comparable values of the thermal conductivities of these materials. Consequently, the resulting temperature gradient in Figs. 5(c) and 5(d) is relatively small, and the resulting nonlinear acoustic body force \mathbf{f}_{ac}^d is so weak that the usual four-roll boundary-driven streaming dominates \mathbf{v}_0 in Fig. 5(f) over the two-roll thermoacoustic bulk-driven streaming, which is dominant in Fig. 2(f). This demonstrates that

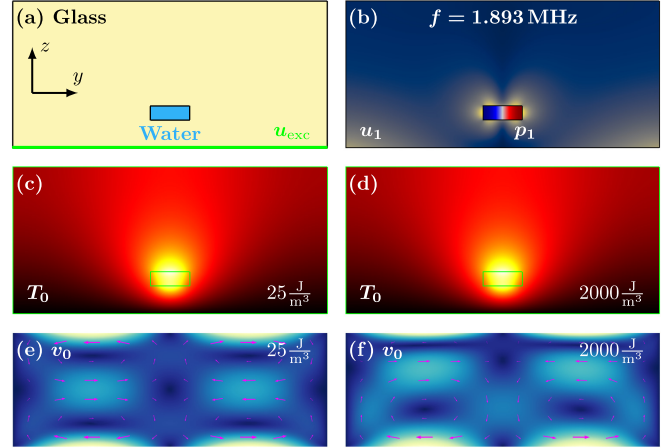


FIG. 5. Study at frequency $f = 1.893 \text{ MHz}$. (a) Sketch of the 2D model of the glass chip with a fluid channel. (b) Color plot at the energy density $E_{ac} = 25 \text{ J/m}^3$ of the displacement $|u_1|$ and pressure p_1 in the fluid. (c) Color plot at $E_{ac} = 25 \text{ J/m}^3$ of the steady temperature field $\Delta T_0 = T_0 - T_0^{\text{bot}}$ from black (0) to yellow (16 mK). (d) Color plot at $E_{ac} = 2000 \text{ J/m}^3$ of ΔT_0 from black (0) to yellow (1.25 K). (e) Vector plot at $E_{ac} = 25 \text{ J/m}^3$ of the streaming \mathbf{v}_0 and color plot of its magnitude v_0 from blue (0) to yellow ($30 \mu\text{m/s}$). (f) Same as (e) but at $E_{ac} = 2000 \text{ J/m}^3$ and with the color scale of v_0 from blue (0) to yellow (2.4 mm/s).

because the inhomogeneous acoustic body force \mathbf{f}_{ac}^d depends on T_0 , it depends on the thermal properties of the surrounding solid and of the placement of heat sink.

C. Example in two dimensions: The influence of the temperature dependency of the fluid properties

The thermal properties of water are distinct compared to most other liquids. In this section, we study the effect of substituting the water in Fig. 2 by rapeseed oil, leaving all other aspects unchanged; see Fig. 6. We chose to study rapeseed oil, because its sound speed is close to that of water, which results in nearly the same horizontal half-wave resonance frequency. However, in contrast to water, its compressibility increases and its sound speed decreases with temperature. As a result, the inhomogeneous acoustic body force \mathbf{f}_{ac}^d points towards the cold instead of the warm temperature region. Rapeseed oil has sound speed $c = 1451 \text{ m/s}$, compressibility $\kappa_T = 5.14 \cdot 10^{-10} \text{ Pa}^{-1}$, viscosity $\eta = 0.047 \text{ Pa}\cdot\text{s}$, and density $\rho = 924 \text{ kg/m}^3$. Moreover, $\alpha_p = 6.61 \cdot 10^{-4} \text{ K}^{-1}$, $\partial_T \rho = -0.65 \text{ kg/(m}^3\text{K)}$, and $\partial_T c = -3.25 \text{ m/(sK)}$ [35]. The frequency of the horizontal half-wave resonance is $f = 1.860 \text{ MHz}$.

When comparing the simulation results of the water-system in Fig. 2 with the oil-system in Fig. 6, we find nearly the same qualitative and quantitative feature, with one notable exception: The direction of the two-roll thermoacoustic bulk-driven streaming at high E_{ac} in Fig. 6(f) is opposite to the corresponding one in Fig. 2(f), whereas the direction of the usual four-roll boundary-driven streaming at low E_{ac} in Fig. 6(e) is the same as the corresponding one in Fig. 2(e). This is as expected: the boundary-driven streaming in the perturbation regime at low E_{ac} is independent of the temperature

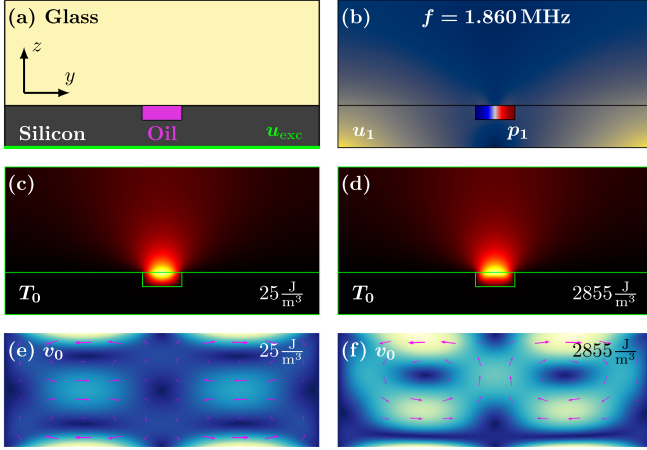


FIG. 6. Study at frequency $f = 1.860$ MHz. (a) Sketch of the 2D model of the glass-silicon chip with a oil channel. (b) Color plot at the energy density $E_{ac} = 25 \text{ J/m}^3$ of the displacement $|\mathbf{u}_1|$ and pressure p_1 in the fluid. (c) Color plot at $E_{ac} = 25 \text{ J/m}^3$ of the steady temperature field $\Delta T_0 = T_0 - T_0^{\text{bot}}$ from black (0) to yellow (95 mK). (d) Color plot at $E_{ac} = 2855 \text{ J/m}^3$ of ΔT_0 from black (0) to yellow (10 K). (e) Vector plot at $E_{ac} = 25 \text{ J/m}^3$ of the streaming \mathbf{v}_0 and color plot of its magnitude v_0 from blue (0) to yellow (30 $\mu\text{m/s}$). (f) Same as (e) but at $E_{ac} = 2855 \text{ J/m}^3$ and with the color scale of v_0 from blue (0) to yellow (3.5 mm/s).

dependencies, whereas the thermoacoustic bulk streaming dominating in the nonperturbative regime at high E_{ac} depends on the sign of the thermal coefficients a_g^T of Eq. (7), which have opposite sign for water and rapeseed oil.

D. Example in three dimensions: Nonlinear thermoacoustic streaming driven by absorption of light

The effective boundary conditions greatly reduce the computational memory requirements, which combined with the iterative solver makes it possible to simulate highly nonlinear effects in 3D systems. As an example, we choose the system in which we previously did both experimental and numerical studies of the temperature-gradient-induced thermoacoustic streaming [8]. In that study, the applied perturbative model was at the limit of its validity because of the high streaming velocity. The application of the nonperturbative iterative effective model on this system not only provides a demonstration example of the ability of the model to simulate 3D systems, but it also allows us to examine specifically the nonperturbative impact of thermal convection in the system at high streaming velocities.

The system, sketched in Fig. 7(a), is a glass-silicon-glass chip with a long rectangular water-filled channel of width $W_{\text{fl}} = 760 \mu\text{m}$ and height $H_{\text{fl}} = 360 \mu\text{m}$, such that the top and bottom of the fluidic channel is in contact with glass and the sides are in contact with silicon. The chip is actuated anti-symmetrically around the xz plane and symmetrically around the yz plane at a frequency $f_0 = 0.957$ MHz by $\mathbf{u}_{\text{exc}} = \mathbf{u}_1^{\text{top}} = d_0 \mathbf{e}_z$ for $0 < x < \frac{1}{2}L_{\text{PZT}}$ and $\frac{1}{2}W < y < \frac{1}{2}W_{\text{sl}}$ at the top surface, which excites the half-wave resonance in the width of the channel. Dye has been added to the water to absorb the light from a light-emitting diode (LED). The absorbed light heats

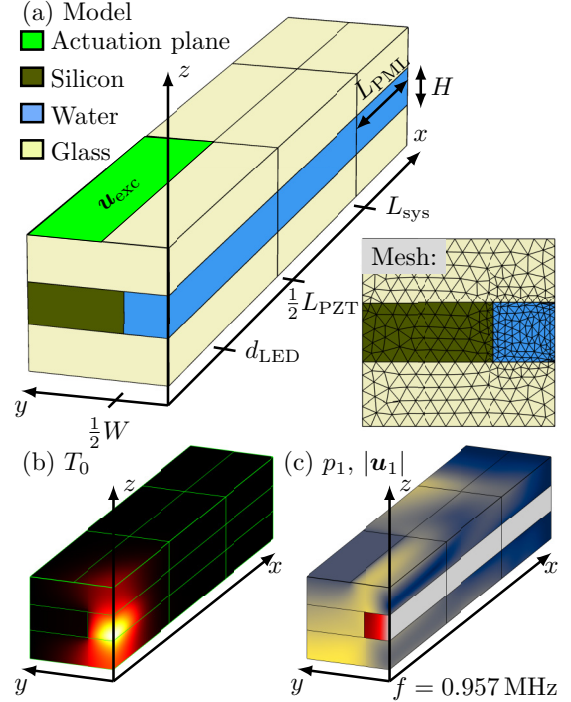


FIG. 7. (a) Domain for simulating T_0 , p_1 , and $|\mathbf{u}_1|$ in a quarter of the glass-Si-glass system, actuated at the top (green) by $\mathbf{u}_{\text{exc}} = \mathbf{u}_1^{\text{top}} = d_0 \mathbf{e}_z$ for $0 < x < \frac{1}{2}L_{\text{PZT}}$, $\frac{1}{2}W < y < \frac{1}{2}W_{\text{sl}}$, and $z = z_{\text{top}}$. The system is studied at the horizontal half-wave resonance in the channel at $f = 0.957$ MHz. (b) Color plot of T_0 from 20°C (black) to 20.8°C (yellow) due to the absorption of light from an LED with $P = 5$ mW. (c) Color plot of the acoustic displacement $|\mathbf{u}_1|$ from 0 nm (blue) to 18 nm (yellow) in the solid, and the acoustic pressure p_1 in the water-filled $0.76 \times 0.36 \text{ mm}^2$ microchannel from 0 MPa (gray) to 1.2 MPa (red).

up the water and induces a temperature gradient ∇T_0 , which spawns an acoustic body force \mathbf{f}_{ac}^d [Eq. (51)] in the bulk, and a heat sink keeps a fixed $T_0 = 20^\circ\text{C}$ at the silicon wall. As a result, high thermoacoustic streaming and thermal convection appear. In contrast to the 2D example of Sec. VIA, we keep the acoustic energy density E_{ac} constant in the 3D example and vary only the power of the LED. The acoustic body force \mathbf{f}_{ac}^d , and thus the streaming velocity \mathbf{v}_0 , depends linearly on ∇T_0 . Consequently, if the thermal convection is negligible, \mathbf{v}_0 depends linearly on the LED power.

In the numerical model, we use symmetry planes and perfectly matched layers (PML) to reduce the size of the 3D model. The LED is placed in the center of the channel, so both the yz plane at $x = 0$ and the xz plane at $y = 0$ are symmetry planes. On the yz plane all steady and acoustic fields are symmetric, whereas on the xz plane the steady fields as well as the u_x and u_z component of the displacement field are symmetric, and the acoustic pressure p_1 and the u_y component of the displacement field are antisymmetric. The two symmetry planes are used to reduce the system to a quarter as shown in Fig. 7. The PML layer is used to dampen waves traveling along the x -axis away from the center, and it allows us to restrict the computational domain to the region closest to the LED spot.

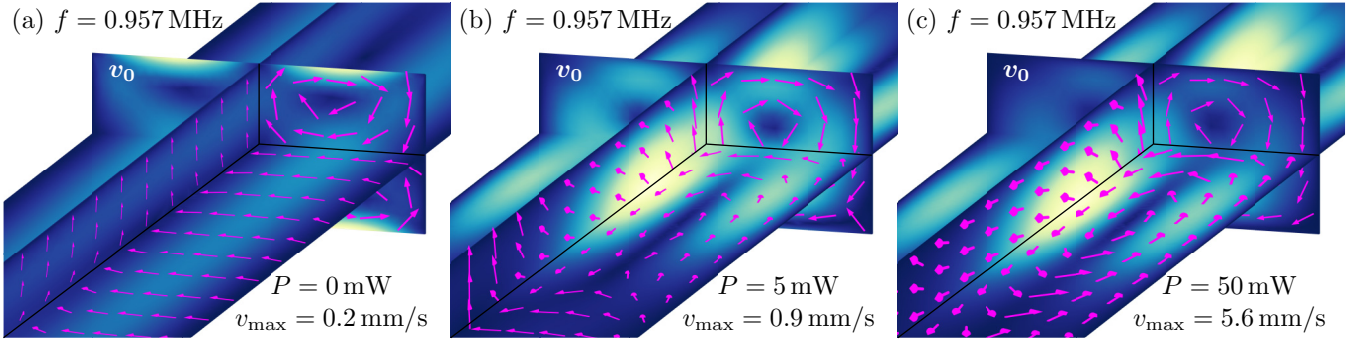


FIG. 8. Simulated streaming \mathbf{v}_0 at acoustic energy density $E_{ac} = 150 \text{ J/m}^3$ and frequency $f = 0.957 \text{ MHz}$ for the LED power $P = 0, 5,$ and 50 mW , respectively. The color plots from 0 mm/s (blue) to v_{\max} (yellow) are the in-plane velocity of the respective planes, on the yz plane it is $(v_{0,y}^2 + v_{0,z}^2)^{1/2}$, and likewise for the xy and xz planes. All arrows are unit vectors showing the direction of \mathbf{v}_0 . (a) \mathbf{v}_0 for $P = 0 \text{ mW}$ showing the usual four boundary-driven streaming rolls with $v_{\max} = 0.2 \text{ mm/s}$. (b) \mathbf{v}_0 for $P = 5 \text{ mW}$ showing a slightly dominant thermoacoustic streaming flow with $v_{\max} = 0.9 \text{ mm/s}$ driven by the acoustic body force \mathbf{f}_{ac}^d (51) in the bulk. (c) \mathbf{v}_0 for $P = 50 \text{ mW}$ completely dominated by the fast streaming flow with $v_{\max} = 5.6 \text{ mm/s}$ driven by the acoustic body force \mathbf{f}_{ac}^d in the bulk.

For the streaming \mathbf{v}_0 , a boundary condition of no-slip is used at the PML. This boundary condition is unphysical, but it does not alter the streaming at the vicinity of the LED spot. Further details on the implementation of the PML layer and boundary conditions on the symmetry plane can be found in the Supplemental Material [37].

The amplitude of the actuation displacement \mathbf{u}_{exc} is chosen to fix the acoustic energy density to $E_{ac} = 150 \text{ J/m}^3$ at $x = 0$, and the LED is modeled to be a Gaussian beam centered at $x = y = 0$ and with a width of $650 \mu\text{m}$. With a LED power of $P = 5 \text{ mW}$, the resulting steady temperature field T_0 and acoustic pressure p_1 and displacement field \mathbf{u}_1 are shown in Fig. 7. T_0 is highest at the bottom of the fluidic channel, because the light is absorbed there, and the silicon side walls keep the temperature of the channel sides low by transporting the heat to a heat sink kept at 20°C .

When the LED is off, \mathbf{v}_0 is dominated by the usual boundary-driven streaming, but when it is on, \mathbf{v}_0 is dominated by the thermoacoustic streaming driven by the acoustic body force \mathbf{f}_{ac}^d . The transition from boundary- to bulk-driven streaming is thoroughly studied in Ref. [8]. The resulting \mathbf{v}_0 for three different LED powers are shown in Fig. 8. Here the solution computed in the quarter of the channel has been mirrored in the two symmetry planes to obtain \mathbf{v}_0 in the full channel. In Fig. 8(a) is shown the classical boundary-driven Rayleigh streaming for zero LED power, $P = 0 \text{ mW}$. In this case, the streaming pattern contains four characteristic 2D streaming rolls in the yz plane, similar to \mathbf{v}_0 in Fig. 2(e), with almost no flow in the x direction. In Fig. 8(b) is shown the streaming for moderate LED power, $P = 5 \text{ mW}$, with a maximum velocity of 0.9 mm/s , which recovers the 3D flow pattern driven by the bulk acoustic body force \mathbf{f}_{ac}^d as observed in Ref. [8]. In Fig. 8(c) is shown the streaming for high LED power, $P = 50 \text{ mW}$, with a maximum velocity of 5.6 mm/s . This pattern looks like the one for $P = 5 \text{ mW}$, but is slightly deformed due to changes in ∇T_0 and thus in \mathbf{f}_{ac}^d due to non-linear thermal convection.

The temperature fields for $P = 5$ and 50 mW are shown in Figs. 9(a) and 9(b) in the yz plane at $x = 0$. In the case of

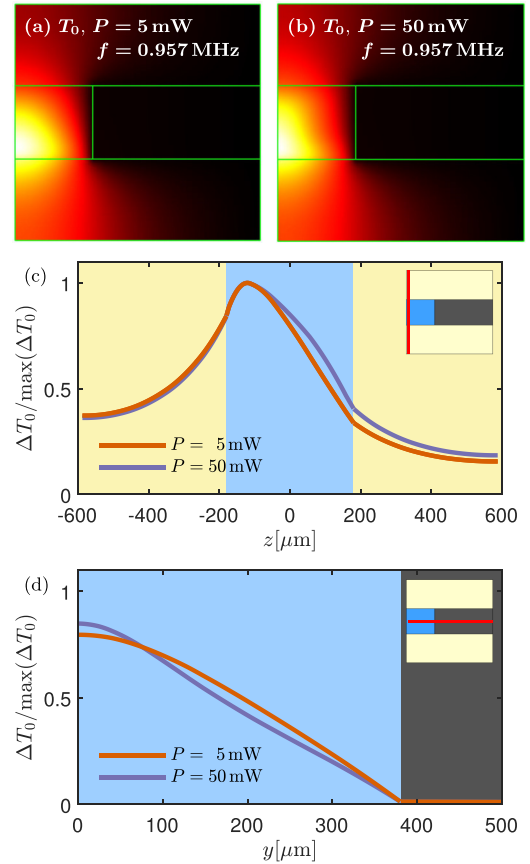


FIG. 9. Convection due to high streaming velocities at $f = 0.957 \text{ MHz}$. (a) The temperature field in the yz plane at $x = 0$ generated by the light absorption from a LED of power $P = 5 \text{ mW}$ ranging from $T_0 = 20.0^\circ\text{C}$ (black) to $T_0 = 20.8^\circ\text{C}$ (yellow). (b) Same as (a) but for $P = 50 \text{ mW}$ and a color range from $T_0 = 20.0^\circ\text{C}$ (black) to $T_0 = 27.3^\circ\text{C}$ (yellow). (c) A line plot of the two normalized temperature fields along a line at $x = y = 0$ shown in the inset. (d) A line plot of the two normalized temperature fields along a line at $x = z = 0$ shown in the inset. The differences in the two temperature fields are due to convection.

$P = 50$ mW, the streaming-induced convection has stretched the temperature field up along the center axis and thereby altering T_0 and f_{ac}^d . This stretching reduces the temperature gradient and f_{ac} along z , and therefore leads to the reduction of \mathbf{v}_0 in the vertical yz plane relative to the one in the horizontal xy plane seen when comparing Figs. 8(b) to 8(c). The dependence of the ΔT_0 profile on the LED power P is quantified by the line plots of the temperature along the vertical line $y = x = 0$ in Fig. 9(c) and the horizontal line $x = z = 0$ in Fig. 9(d). The line plots show that in this nonperturbative regime, the heat convection from the hot to the cold region is strong enough to alter the temperature profile. A similar tendency is also observed in Fig. 4 for the 2D model.

When simulating convection-diffusion processes, the numerical mesh needs to satisfy the stability condition $Pe_{num} = h_{mesh} v_0 / (2D_0^{th}) \lesssim 1$ on the numerical Péclet number Pe_{num} , which restricts the size h_{mesh} of the mesh elements. In this system, with $D_0^{th} \approx 2 \times 10^{-7}$ m²/s and $v_0 = 5.6$ mm/s, we find $h_{mesh} \lesssim 40$ μ m. Consequently, in systems with a high streaming velocity, a fine mesh is required in the bulk, which quickly can make numerical 3D simulation computationally very expensive, even when using the effective boundary-layer model. It is possible to numerically stabilize the diffusion-advection equations to enable simulations with a coarser mesh, but this we have not yet implemented in our simulation.

VII. CONCLUSIONS

We have presented a nonperturbative, effective boundary-layer model for thermoviscous acoustofluidics, which enables simulations of high acoustic energies in three dimensions. The model differs from previous acoustofluidic models [2,5] on two main points: (1) it takes the thermal boundary layers into account analytically in the form of an effective boundary condition for the steady bulk temperature field, which enables 3D simulations of acoustic heating in thermoviscous acoustofluidics, and which makes simulation of thermoviscous systems as computationally cheap as inviscid systems, and (2) it relies on an iterative solver, which incorporate nonperturbative effects and thus allows simulations at higher acoustic energy densities beyond the perturbative regime of conventional models.

General physical aspects and an experimental validation of the *full* model is presented in Ref. [9], whereas here we have given a detailed presentation of both the *full* and the *effective boundary-layer* iterative model as well as studied four simulation examples for typical acoustofluidic devices, each emphasizing a particular physical aspect of the model, thus demonstrating its potential. (1) In Figs. 2 and 3 of Sec. VIA, the *effective* iterative model was validated against its *full*-model counterpart. The internal acoustic heating due to friction was shown in Figs. 2(c), 2(d), and 3 to be of the order 9–230 mK depending on E_{ac} , and specific nonperturbative effects was studied at $E_{ac} = 2680$ J/m³ for \mathbf{v}_0 in Figs. 2(e) and 2(f) and for T_0 at $E_{ac} = 9000$ J/m³ in Fig. 4. The material dependency on the nonperturbative thermoacoustic streaming was presented Secs. VIB and VIC. (2) By substituting the silicon-glass system in Fig. 2 by the glass-glass system in Fig. 5, it was shown how the thermoacoustic streaming remained in the perturbative regime even at $E_{ac} = 2000$ J/m³.

(3) By substituting the water in Fig. 2 by oil in Fig. 6, it was shown how the thermoacoustic streaming in the nonperturbative regime at $E_{ac} = 2000$ J/m³ changed its direction. (4) Finally, the capability of simulating nonlinear effects in 3D systems in the nonperturbative regime was demonstrated in Sec. VID, which specifically focus on the importance of convective heat transport in a acoustofluidic device with externally controlled temperature gradients.

In many applications of acoustofluidic devices, as high a throughput as possible is desired. Generally, an increased acoustic energy density E_{ac} will allow for an increased throughput. Since the presented iterative model does allow simulations at higher E_{ac} in the nonperturbative regime, it will likely contribute to an increased understanding of nonlinear effects in acoustofluidics, including the four examples studied in this work and the ones [25–27] mentioned in the introduction, and to an improved design capability of acoustofluidic devices with a higher throughput.

ACKNOWLEDGMENT

This work was supported by Independent Research Fund Denmark, Natural Sciences (Grant No. 8021-00310B).

APPENDIX: REDUCTION AND INTEGRATION

In this Appendix, we present the mathematical steps going from Eq. (40) to Eqs. (41a) and (41b) for the heat flux and the temperature in the fluid at the fluid-solid interface. Beginning with Eq. (40), but suppressing the superscript “fl” for simplicity, we have

$$k_0^{th} \partial_z^2 T_0^\delta = -\nabla \cdot (\langle k_1^{th} \nabla T_1 \rangle^\delta + \langle \mathbf{v}_1 \cdot \boldsymbol{\tau}_1 \rangle^\delta - \langle p_1 \mathbf{v}_1 \rangle^\delta - \rho_0 c_{p0} \langle T_1 \mathbf{v}_1 \rangle^\delta), \quad (A1)$$

where each term $\langle \dots \rangle^\delta$ contains at least one boundary layer field T_1^δ or \mathbf{v}_1^δ . First, the four terms on the right-hand side are evaluated and reduced one by one. Then they are integrated with respect to z , once to find $-k_0^{th} \partial_z T_0^\delta$, and twice to find T_0^δ , which both are needed for the boundary conditions in Eqs. (39a) and (39b). Similarly, we repeatedly use in the following that gradient terms are dominated by z derivatives of boundary-layer fields T_1^δ , \mathbf{v}_1^δ , and $\mathbf{v}_1^{d,T}$, as each such derivative results in a factor $(k_c \delta)^{-1} \gg 1$. We also note that $\langle (ip_1) p_1 \rangle = \langle (iT_1) T_1 \rangle = 0$, and another helpful relation is found in Ref. [7], Eq. (33a),

$$\nabla \cdot \mathbf{v}_1 = i(1 - i\Gamma_s) \omega \kappa_{s0} p_1 - i\omega \alpha_{p0} T_1^\delta, \quad (A2)$$

revealing that $\nabla \cdot \mathbf{v}_1$ depends not only on the bulk pressure p_1 but also on the boundary-layer temperature field T_1^δ . Using this insight together with the exponentially decaying boundary-layer fields from Eq. (30), we find for the pressure-generated power,

$$\begin{aligned} \nabla \cdot (\langle p_1 \mathbf{v}_1 \rangle^\delta) &= (\langle \nabla p_1 \cdot \mathbf{v}_1 \rangle^\delta + \langle p_1 \nabla \cdot \mathbf{v}_1 \rangle^\delta) \\ &\approx \frac{\omega}{2} [\rho_0 \text{Re}(i \mathbf{v}_1^{d,p} \cdot \mathbf{v}_1^{\delta*}) + \alpha_{p0} \text{Re}(ip_1 T_1^{\delta*})]. \end{aligned} \quad (A3)$$

The first term, being of the order $\omega\rho_0v_1^2 \approx \omega\kappa_{s0}p_1^2$, turns out to be the dominant term. Likewise, for the heat-generated power, we find that

$$\begin{aligned} & \nabla \cdot (c_{p0}\rho_0\langle T_1\mathbf{v}_1\rangle^\delta) \\ & \approx c_p\rho_0[\langle \nabla T_1^\delta \cdot \mathbf{v}_1 \rangle + \langle T_1^\delta(i\omega\kappa_{s0}p_1) \rangle] \\ & \approx \frac{c_p\rho_0}{2}\text{Re}[\langle \nabla T_1^\delta \cdot (\mathbf{v}_1^{\delta*} + \mathbf{v}_1^{d,T*} + \mathbf{v}_1^{d,p*}) - i\omega\kappa_s T_1^\delta p_1^* \rangle]. \end{aligned} \quad (\text{A4})$$

In the stress-generated power $\nabla \cdot \langle \mathbf{v}_1 \cdot \boldsymbol{\tau}_1 \rangle^\delta$, we keep only terms $\partial_z v_1^\delta$, each producing a factor of $(k_c\delta)^{-1} \gg 1$. Thus, $\mathbf{v}_1 \cdot \boldsymbol{\tau}_1 \approx \eta_0[v_{1z}(\partial_z v_1^\delta) + (\mathbf{v}_1 \cdot \partial_z \mathbf{v}_1^\delta)\mathbf{e}_z]$ gives

$$\begin{aligned} & \nabla \cdot \langle \mathbf{v}_1 \cdot \boldsymbol{\tau}_1 \rangle^\delta \\ & \approx \eta_0 \nabla \cdot \langle v_{1z}(\partial_z v_1^\delta) \rangle + \eta_0 \partial_z \langle \mathbf{v}_1 \cdot (\partial_z \mathbf{v}_1^\delta) \rangle \\ & \approx \eta_0 [(\partial_z v_{1z}^\delta)^2 + \langle |\partial_z \mathbf{v}_1^\delta|^2 \rangle + \langle \mathbf{v}_1 \cdot \partial_z^2 \mathbf{v}_1^\delta \rangle] \\ & = \frac{\eta_0}{2} \text{Re} [|k_s|^2 v_{1z}^\delta v_{1z}^{\delta*} + |k_s|^2 \mathbf{v}_1^\delta \cdot \mathbf{v}_1^{\delta*} - (k_s^*)^2 \mathbf{v}_1 \cdot \mathbf{v}_1^{\delta*}] \\ & = \frac{\rho_0\omega}{2} \text{Re} [v_{1z}^\delta v_{1z}^{\delta*} + \mathbf{v}_1^\delta \cdot \mathbf{v}_1^{\delta*} + i\mathbf{v}_1^{d,p} \cdot \mathbf{v}_1^{\delta*}]. \end{aligned} \quad (\text{A5})$$

Here we have used that $\text{Re}[i\mathbf{v}_1^\delta \cdot \mathbf{v}_1^{\delta*}] = 0$, and that $k_s = (1+i)\delta_s^{-1}$ implies the relations $(k_s^*)^2 = -i2\delta_s^{-2}$, $|k_s|^2 = 2\delta_s^{-2}$, and $2\eta_0\delta_s^{-2} = \rho_0\omega$.

The last term is the power generated by thermal conduction, which only contains the thermal boundary layer characterized by the wave number $k_t = (1+i)\delta_t^{-1}$ [Eq. (28)]

$$\begin{aligned} & \nabla \cdot \langle k_1^{\text{th}} \nabla T_1 \rangle^\delta \approx \langle (\partial_z k_1^{\text{th}}) \partial_z T_1^\delta \rangle + \langle k_1^{\text{th}} \partial_z^2 T_1^\delta \rangle \\ & = \frac{1}{2} \text{Re} [k_t k_t^* k_1^{\text{th},\delta} T_1^{\delta*} - (k_1^{\text{th},d} + k_1^{\text{th},\delta}) (k_t^*)^2 T_1^{\delta*}] \\ & = \frac{1}{\delta_t^2} \text{Re} [(1+i) k_1^{\text{th},\delta} T_1^{\delta*} + i k_1^{\text{th},d} T_1^{\delta*}]. \end{aligned} \quad (\text{A6})$$

For water, this term is a factor $(\gamma-1)a_k\alpha_{p0}T_0 \approx 10^{-2}$ smaller than $\omega\kappa_{s0}p_1^2$, as can be seen by using $\delta_t^{-2}k_1^{\text{th}} \approx \omega\rho_0c_p k_1^{\text{th}}/k_0^{\text{th}} \approx \omega\rho_0c_p a_k \alpha_{p0} T_1 = a_k \omega \alpha_{p0}^2 T_0 p_1$ and $T_1 \approx (\gamma-1)(\kappa_{s0}/\alpha_{p0}) p_1$. So the power generated by thermal conduction can be neglected in fluids, but it may be important for gases. Inserting the power contributions (A3)–(A6) into Eq. (A1), we arrive at the expression

$$\begin{aligned} & k_0^{\text{th}} \partial_z^2 T_0^\delta \\ & = -\frac{\omega\rho_0}{2} \text{Re}(\mathbf{v}_1^\delta \cdot \mathbf{v}_1^{\delta*}) + \frac{\omega\alpha_{p0}}{2} \text{Re}(ip_1 T_1^{\delta*}) \\ & \quad + \frac{c_p\rho_0}{2} \text{Re}[\langle \nabla T_1^\delta \cdot (\mathbf{v}_1^{\delta*} + \mathbf{v}_1^{d,T*} + \mathbf{v}_1^{d,p*}) - i\omega\kappa_s T_1^\delta p_1^* \rangle] \\ & \quad - \frac{\omega c_p \rho_0}{k_0^{\text{th}}} \text{Re}[(1+i)k_1^{\text{th},\delta} T_1^{\delta*} + ik_1^{\text{th},d} T_1^{\delta*}], \end{aligned} \quad (\text{A7})$$

where the first term is the leading term, which originates from the viscous boundary layer. This expression is now integrated from $z = \infty$ to $z = 0$ once to obtain the heat flux and twice to obtain the boundary-layer temperature at the interface. The fields in the boundary layer are well approximated by surface

fields that does not depend on the normal coordinate z but only on the in-plane coordinates x and y , according to the following separations:

$$\begin{aligned} p_1^d &= p_1^{d0}(x, y), & T_1^{\text{fl},\delta} &= T_1^{\text{fl},\delta 0}(x, y)r(z), \\ \mathbf{v}_1^{d,p} &= \mathbf{v}_1^{d0,p}(x, y), & T_1^{\text{sl},\delta} &= T_1^{\text{sl},\delta 0}(x, y)r^*(z), \\ \mathbf{v}_1^\delta &= \mathbf{v}_1^{\delta 0}(x, y)q(z), & \mathbf{v}_1^{d,T} &= \alpha_{p0} D_0^{\text{th}} \nabla [T_1^{\text{fl},\delta 0}(x, y)r(z)], \\ q(z) &= e^{ik_{sz}}, & r(z) &= e^{ik_{tz}}. \end{aligned} \quad (\text{A8})$$

Inserting this into Eq. (A7), we obtain

$$\begin{aligned} & k_0^{\text{th}} \partial_z^2 T_0^\delta \\ & = \frac{1}{2} \omega \rho_0 \text{Re} \left\{ -\mathbf{v}_1^{\delta 0} \cdot \mathbf{v}_1^{\delta 0*} q q^* + i \frac{\omega \alpha_{p0}}{\rho_0} p_1^0 T_1^{\delta 0*} r^* \right. \\ & \quad + \frac{c_p}{\omega} [\nabla_{\parallel} T_1^{\delta 0} \cdot \mathbf{v}_{1,\parallel}^{\delta 0*} q^* + ik_t T_1^{\delta 0} (v_{1,z}^{\delta 0*} q^* + v_{1,z}^{d,T0*} r^*)] r \\ & \quad + \frac{c_p}{\omega} [\nabla_{\parallel} T_1^{\delta 0} \cdot \mathbf{v}_{1,\parallel}^{d,p0*} + ik_t T_1^{\delta 0} v_{1,z}^{d,p0*} - i\omega\kappa_s T_1^{\delta 0} p_1^0] r \\ & \quad \left. - \frac{c_p}{k_0^{\text{th}}} [(1+i)k_1^{\text{th},\delta 0} r + ik_1^{\text{th},d0}] r^* T_1^{\delta 0*} \right\}. \end{aligned} \quad (\text{A9})$$

When integrating Eq. (A9) with respect to z , the xy -dependent surface fields (superscript “0”) move outside the integral. Using the procedure of Ref. [5], we introduce the integrals $I_{ab}^{(n)}$ of the integrand $a(z)b(z)^*$, where $a(z)$ and $b(z)$ are any of the functions 1, $q(z)$, and $r(z)$:

$$\begin{aligned} I_{ab}^{(n)} &= \int^z dz_n \int^{z_n} dz_{n-1} \cdots \int^{z_2} dz_1 a(z_1) b(z_1)^* \Big|_{z=0}, \\ I_{ab}^{(n)} &\propto \delta^n, \text{ with } \delta = \delta_s, \delta_t \text{ and } n = 1, 2, 3, \dots \end{aligned} \quad (\text{A10})$$

Integrating Eq. (A9) once with respect to z thus gives

$$\begin{aligned} & \partial_z T_0^\delta \\ & = \frac{1}{2D_0^{\text{th}}} \text{Re} \left\{ -\frac{\omega}{c_p} \mathbf{v}_1^{\delta 0} \cdot \mathbf{v}_1^{\delta 0*} I_{qq}^{(1)} + i \frac{\omega \alpha_{p0}}{c_p \rho_0} p_1^0 T_1^{\delta 0*} I_{r^*}^{(1)} \right. \\ & \quad + (\nabla_{\parallel} T_1^{\delta 0} \cdot \mathbf{v}_{1,\parallel}^{\delta 0*} + ik_t T_1^{\delta 0} v_{1,z}^{\delta 0*}) I_{rq}^{(1)} + ik_t T_1^{\delta 0} v_{1,z}^{d,T0*} I_{rr}^{(1)} \\ & \quad + (\nabla_{\parallel} T_1^{\delta 0} \cdot \mathbf{v}_{1,\parallel}^{d,p0*} + ik_t T_1^{\delta 0} v_{1,z}^{d,p0*} - i\omega\kappa_s T_1^{\delta 0} p_1^0) I_{r^*}^{(1)} \\ & \quad \left. - \frac{\omega}{k_0^{\text{th}}} [(1+i)k_1^{\text{th},\delta 0} I_{rr}^{(1)} + ik_1^{\text{th},d0} I_{r^*}^{(1)}] T_1^{\delta 0*} \right\}. \end{aligned} \quad (\text{A11})$$

Inserting here the values of $I_{ab}^{(1)}$ given by

$$\begin{aligned} I_{r^*}^{(1)} &= -\frac{1+i}{2} \delta_t, & I_{rr}^{(1)} &= -\frac{1}{2} \delta_t, & I_{ba}^{(n)} &= [I_{ab}^{(n)}]^*, \\ I_{rq}^{(1)} &= -\frac{1+i}{2} \frac{\delta_s \delta_t}{\delta_s + i\delta_t}, & I_{qq}^{(1)} &= -\frac{1}{2} \delta_s, \end{aligned} \quad (\text{A12})$$

leads to $\partial_z T_0^{\text{fl},\delta 0}$ at the fluid-solid interface:

$$\begin{aligned} \partial_z T_0^{\text{fl},\delta 0} &= \text{Re} \left(\frac{1+i}{4D_0^{\text{th}}} \left\{ \frac{1-i}{2} \frac{\delta_s \omega}{c_p} \mathbf{v}_1^{\delta 0} \cdot \mathbf{v}_1^{\delta 0*} - \frac{\delta_t \omega \alpha_{p0}}{c_p \rho_0} p_1^0 T_1^{\delta 0*} \right. \right. \\ & \quad \left. \left. - \frac{\delta_s}{\delta_s + i\delta_t} [\delta_t \nabla_{\parallel} T_1^{\delta 0} \cdot \mathbf{v}_{1,\parallel}^{\delta 0*} - (1-i) T_1^{\delta 0} v_{1,z}^{\delta 0*}] \right\} \right) \end{aligned}$$

$$\begin{aligned}
 & -iT_1^{\delta 0} \left[v_{1,z}^{d,T0*} + (1+i)v_{1,z}^{d,p0*} - \delta_t \omega \kappa_s p_1^{0*} \right] \\
 & - \delta_t \nabla_{\parallel} T_1^{\delta 0} \cdot v_{1,\parallel}^{d,p0*} + \delta_t \omega \frac{k_1^{\text{th},\delta 0} + k_1^{\text{th},d0}}{k_0^{\text{th}}} T_1^{\delta 0*} \Bigg\}. \tag{A13}
 \end{aligned}$$

To obtain the temperature $T_0^{\delta 0}$ at the fluid-solid interface, we integrate Eq. (A9) twice with respect to z . This is easily done by changing $I_{ab}^{(1)}$ to $I_{ab}^{(2)}$ in Eq. (A11) followed by insertion of the values

$$\begin{aligned}
 I_{r1}^{(2)} &= \frac{i}{2} \delta_t^2, & I_{rr}^{(2)} &= \frac{1}{4} \delta_t^2, \\
 I_{rq}^{(2)} &= \frac{i}{2} \frac{\delta_s^2 \delta_t^2}{(\delta_s + i\delta_t)^2}, & I_{qq}^{(2)} &= \frac{1}{4} \delta_s^2. \tag{A14}
 \end{aligned}$$

The result for $T_0^{\text{fl},\delta 0}$ becomes

$$\begin{aligned}
 T_0^{\text{fl},\delta 0} &= \frac{\delta_t}{4D_0^{\text{th}}} \text{Re} \left\{ -\frac{\delta_s^2 \omega}{2\delta_t c_p} v_1^{\delta 0} \cdot v_1^{\delta 0*} + \frac{\delta_t \omega \alpha p_0}{c_p \rho_0} p_1^0 T_1^{\delta 0*} \right. \\
 &+ i \frac{\delta_s^2}{(\delta_s + i\delta_t)^2} \left[\delta_t \nabla_{\parallel} T_1^{\delta 0} \cdot v_{1,\parallel}^{\delta 0*} - (1-i) T_1^{\delta 0} v_{1,z}^{\delta 0*} \right] \\
 &- T_1^{\delta 0} \left[\frac{1-i}{2} v_{1,z}^{d,T0*} + (1+i) v_{1,z}^{d,p0*} - \delta_t \omega \kappa_s p_1^{0*} \right] \\
 &\left. + i \delta_t \nabla_{\parallel} T_1^{\delta 0} \cdot v_{1,\parallel}^{d,p0*} - \delta_t \omega \frac{(1+i)k_1^{\text{th},\delta 0} + 2k_1^{\text{th},d0}}{2k_0^{\text{th}}} T_1^{\delta 0*} \right\}. \tag{A15}
 \end{aligned}$$

Again the first term is the leading term that originates from the viscous boundary layer.

[1] P. B. Muller, R. Barnkob, M. J. H. Jensen, and H. Bruus, A numerical study of microparticle acoustophoresis driven by acoustic radiation forces and streaming-induced drag forces, *Lab Chip* **12**, 4617 (2012).

[2] P. B. Muller and H. Bruus, Numerical study of thermoviscous effects in ultrasound-induced acoustic streaming in microchannels, *Phys. Rev. E* **90**, 043016 (2014).

[3] P. Hahn and J. Dual, A numerically efficient damping model for acoustic resonances in microfluidic cavities, *Phys. Fluids* **27**, 062005 (2015).

[4] P. Hahn, I. Leibacher, T. Baasch, and J. Dual, Numerical simulation of acoustofluidic manipulation by radiation forces and acoustic streaming for complex particles, *Lab Chip* **15**, 4302 (2015).

[5] J. S. Bach and H. Bruus, Theory of pressure acoustics with viscous boundary layers and streaming in curved elastic cavities, *J. Acoust. Soc. Am.* **144**, 766 (2018).

[6] N. R. Skov, J. S. Bach, B. G. Winkelmann, and H. Bruus, 3D modeling of acoustofluidics in a liquid-filled cavity including streaming, viscous boundary layers, surrounding solids, and a piezoelectric transducer, *AIMS Math.* **4**, 99 (2019).

[7] J. H. Joergensen and H. Bruus, Theory of pressure acoustics with thermoviscous boundary layers and streaming in elastic cavities, *J. Acoust. Soc. Am.* **149**, 3599 (2021).

[8] W. Qiu, J. H. Joergensen, E. Corato, H. Bruus, and P. Augustsson, Fast Microscale Acoustic Streaming Driven by a Temperature-Gradient-Induced Non-Dissipative Acoustic Body Force, *Phys. Rev. Lett.* **127**, 064501 (2021).

[9] J. H. Joergensen, W. Qiu, and H. Bruus, Transition from Boundary-Driven to Bulk-Driven Acoustic Streaming Due to Nonlinear Thermoviscous Effects at High Acoustic Energy Densities, *Phys. Rev. Lett.* **130**, 044001 (2023).

[10] J. Rufo, F. Cai, J. Friend, M. Wiklund, and T. J. Huang, Acoustofluidics for biomedical applications, *Nat. Rev. Methods Primers* **2**, 30 (2022).

[11] J. T. Karlsen, P. Augustsson, and H. Bruus, Acoustic Force Density Acting on Inhomogeneous Fluids in Acoustic Fields, *Phys. Rev. Lett.* **117**, 114504 (2016).

[12] J. D. Adams, C. L. Ebbesen, R. Barnkob, A. H. J. Yang, H. T. Soh, and H. Bruus, High-throughput, temperature-controlled microchannel acoustophoresis device made with rapid prototyping, *J. Micromech. Microeng.* **22**, 075017 (2012).

[13] Y. Chen, M. Wu, L. Ren, J. Liu, P. H. Whitley, L. Wang, and T. J. Huang, High-throughput acoustic separation of platelets from whole blood, *Lab Chip* **16**, 3466 (2016).

[14] M. Antfolk and T. Laurell, Continuous flow microfluidic separation and processing of rare cells and bioparticles found in blood—A review, *Anal. Chim. Acta* **965**, 9 (2017).

[15] M. Wu, A. Ozcelik, J. Rufo, Z. Wang, R. Fang, and T. J. Huang, Acoustofluidic separation of cells and particles, *Microsyst. Nanoeng.* **5**, 32, 1 (2019).

[16] R. Barnkob, P. Augustsson, T. Laurell, and H. Bruus, Measuring the local pressure amplitude in microchannel acoustophoresis, *Lab Chip* **10**, 563 (2010).

[17] P. Augustsson, R. Barnkob, S. T. Wereley, H. Bruus, and T. Laurell, Automated and temperature-controlled micro-PIV measurements enabling long-term-stable microchannel acoustophoresis characterization, *Lab Chip* **11**, 4152 (2011).

[18] R. Barnkob, I. Iranmanesh, M. Wiklund, and H. Bruus, Measuring acoustic energy density in microchannel acoustophoresis using a simple and rapid light-intensity method, *Lab Chip* **12**, 2337 (2012).

[19] P. B. Muller, M. Rossi, A. G. Marin, R. Barnkob, P. Augustsson, T. Laurell, C. J. Kähler, and H. Bruus, Ultrasound-induced acoustophoretic motion of microparticles in three dimensions, *Phys. Rev. E* **88**, 023006 (2013).

[20] M. Bora and M. Shusteff, Efficient coupling of acoustic modes in microfluidic channel devices, *Lab Chip* **15**, 3192 (2015).

[21] A. Tahmasebipour, L. Friedrich, M. Begley, H. Bruus, and C. Meinhart, Toward optimal acoustophoretic microparticle manipulation by exploiting asymmetry, *J. Acoust. Soc. Am.* **148**, 359 (2020).

[22] F. Lickert, M. Ohlin, H. Bruus, and P. Ohlsson, Acoustophoresis in polymer-based microfluidic devices: Modeling and experimental validation, *J. Acoust. Soc. Am.* **149**, 4281 (2021).

[23] W. Qiu, T. Baasch, and T. Laurell, Enhancement of Acoustic Energy Density in Bulk-Wave-Acoustophoresis Devices Using Side Actuation, *Phys. Rev. Appl.* **17**, 044043 (2022).

[24] G. Michel and G. P. Chini, Strong wave-mean-flow coupling in baroclinic acoustic streaming, *J. Fluid Mech.* **858**, 536 (2019).

- [25] W. Cui, H. Zhang, H. Zhang, Y. Yang, M. He, H. Qu, W. Pang, D. Zhang, and X. Duan, Localized ultrahigh frequency acoustic fields induced micro-vortices for submillisecond microfluidic mixing, *Appl. Phys. Lett.* **109**, 253503 (2016).
- [26] A. Marin, M. Rossi, B. Rallabandi, C. Wang, S. Hilgenfeldt, and C. J. Kähler, Three-Dimensional Phenomena in Microbubble Acoustic Streaming, *Phys. Rev. Appl.* **3**, 041001(R) (2015).
- [27] C. Zhang, X. Guo, L. Royon, and P. Brunet, Unveiling of the mechanisms of acoustic streaming induced by sharp edges, *Phys. Rev. E* **102**, 043110 (2020).
- [28] COMSOL Multiphysics 5.6, <http://www.comsol.com> (2020).
- [29] W. N. Bodé and H. Bruus, Numerical study of the coupling layer between transducer and chip in acoustofluidic devices, *J. Acoust. Soc. Am.* **149**, 3096 (2021).
- [30] L. D. Landau and E. M. Lifshitz, *Theory of Elasticity. Course of Theoretical Physics*, 3rd ed., Vol. 7 (Pergamon Press, Oxford, 1986).
- [31] J. T. Karlsen and H. Bruus, Forces acting on a small particle in an acoustical field in a thermoviscous fluid, *Phys. Rev. E* **92**, 043010 (2015).
- [32] L. D. Landau and E. M. Lifshitz, *Fluid Mechanics*, 2nd ed., Vol. 6 (Pergamon Press, Oxford, 1993).
- [33] L. D. Landau and E. M. Lifshitz, *Statistical Physics, Part 1*, 3rd ed., Vol. 5 (Butterworth-Heinemann, Oxford, 1980).
- [34] P. B. Muller and H. Bruus, Theoretical study of time-dependent, ultrasound-induced acoustic streaming in microchannels, *Phys. Rev. E* **92**, 063018 (2015).
- [35] J. N. Coupland and D. J. McClements, Physical properties of liquid edible oils, *J. Am. Oil Chem. Soc.* **74**, 1559 (1997).
- [36] R. Barnkob, P. Augustsson, T. Laurell, and H. Bruus, Acoustic radiation- and streaming-induced microparticle velocities determined by microparticle image velocimetry in an ultrasound symmetry plane, *Phys. Rev. E* **86**, 056307 (2012).
- [37] See Supplemental Material at <http://link.aps.org/supplemental/10.1103/PhysRevE.107.015106> for details about the implementation of the symmetry planes and PML in the 3D model.